Numerical Study of Flow Control on Simplified High-Lift Configurations

B. Goffert[1], R. G. Silva[2], C. P. F. Francisco[1,2] and M. L. C. C. Reis[1,2†]

[1] *Technological Institute of Aeronautics, São José dos Campos, SP, 12228-900, Brazil*
[2] *Institute of Aeronautics and Space, São José dos Campos, SP, 12224-904, Brazil*

†*Corresponding Author Email: marialuisamlccr@fab.mil.br*

ABSTRACT

Enhancement in the aerodynamic performance of wings and airfoils is very notable when Active Flow Control (AFC) is applied to Short Take-off and Landing aircraft (STOL). The present numerical study shows the application of steady, pulsed and synthetic tangential jets applied to the plain flap shoulder of a modified NASA Trapezoidal Wing. Pulsed jets are modeled by sinusoidal and square waveforms while synthetic jets are modeled only by pure sine waveform. The freestream airflow conditions are Mach number equal to 0.2 and Reynolds number equal to 4.3 million based on the mean aerodynamic chord. The presented simulations are two-dimensional and based on RANS for steady jet cases and URANS for pulsed and synthetic cases, compiled with the open-source suite SU2 and adapted for time varying boundary conditions. Numerical results for modified configurations based on the same baseline wing profile considering different leading edges, jet slot height, flap position, blowing mass flow, type and frequency of the jets are presented. Curves of pressure coefficient distribution revealed a substantial influence upstream of the AFC, around the slat and main element. The jet slot height analysis showed that the lift gain is also influenced by the slot size due to the change of the local flow velocity considering the same blowing momentum coefficient. Regarding the jet frequency, no significant differences on the lift coefficients were found between the reduced frequencies F^+ equal to 1 and 2. Results of aerodynamic loads showed an improved lift coefficient in relation to the baseline airfoil when pulsed and steady jets are employed. Pulsed jets under square waveform were effective even at high deflected flap condition at 50°, with a significant gain in the lift coefficient of 36%, in relation to the uncontrolled case, combined with a drag reduction of 20%, and a decrease in mass flow up to 49% in relation to the steady jet for the same lift gain. Although sine and square waveform results presented similar improvements for lift, the drag is around 15% higher for the former. When compared with the steady jet case, the mass flow reduction is 36% for the sinewave. Synthetic jets with zero-net-mass-flux proved superior to the baseline conventional multi-element airfoil only with deployed flap at 50°, where a modest lift improvement of 5% was observed.

NOMENCLATURE

c	wing chord	S	wing area
C_L	lift coefficient	T	jet period
C_{Lmax}	maximum lift coefficient	t	physical time
C_p	pressure coefficient	V_j	jet velocity
C_μ	blowing momentum coefficient	V_{jmax}	maximum jet velocity
f	actuator frequency	V_∞	free stream velocity
F^+	reduced frequency	x_{te}	distance from actuator to trailing edge
h	slot height	y^+	non-dimensional wall distance
M	Mach number	α	angle of attack
$\dot{m}_j$	blowing mass-flow rate	δ_s	slat deflection
P_0	total pressure	δ_f	flap deflection
q_∞	free stream dynamic pressure	ρ_j	blowing density
Re	Reynolds number	ω	angular frequency

1. INTRODUCTION

1.1. Overview

Recent aircraft studies have focused on both aerodynamic improvements and environmental aspects (Delfs *et al.* 2017; Kauth *et al.* 2017; Diekmann 2019; Lin *et al.* 2019; Wild 2020). Required lower take-off and landing speeds and environmental restrictions (Sellers *et al.* 2002; Anders *et al.* 2004; Couluris *et al.* 2010) are encouraging research centers and aircraft manufacturers to develop new technologies to support efforts towards green aviation and noise reduction policies.

Shape optimizations related only to geometric manipulations of the aircraft may have reached their limits, as pointed out by some authors, (Liu and Zha 2016), which precludes further performance improvements and compliance with critical demands. The conventional multi-element system, composed of leading edge slat, main element and trailing edge flap, is known to enhance the overall aerodynamic performance with the lift coefficient limited to a range from 2.5 to 3.5 (Bushnell and Wygnanski 2020), which may not be sufficient for the recent applications on Short Take-off and Landing aircraft, STOL. Besides the lift increase, the conventional system is penalized in terms of cost and weight due to the volume of parts contained in the assembly system. Rudolph (1996) summarized an estimation of weight, number of parts and cost of multi-element systems for a hypothetical aircraft of 250,000 lb maximum gross weight. Based on this study, a change from a double-slotted flap to a single slotted one would save 2,260 lb, 1,290 parts and US$1.379 million. However, an example of this alteration considering a multi-element airfoil with flap deflected 45° would diminish the lift coefficient from 2.60 to 2.26 (Abbott and Von Doenhoff 1959).

Regarding the environmental aspect, steep take-off and landing at lower speeds can benefit urban airports by reducing noise and gas emissions, which directly impact the efficiency of air traffic and environmental control. Also, the improvement in the lift and drag ratio for take-off could lead to a transport aircraft being equipped with a smaller engine, thereby reducing the fuel burn (Lin *et al.* 2017). According to Masiol and Harrison (2014) the average annual growth rate of 5% in air traffic is expected to continue over the coming decades. This poses questions regarding the consequential impact on air quality, given that the emissions from aircraft engines caused by the operation at full thrust for take-off and 85% for climb are recognized as a major source of pollutants near airports. With the FAA projection that air traffic will increase over the coming years, changes in traffic patterns and glide slopes may be necessary to keep the noise confined to the airport boundaries (Jones *et al.* 2008).

The employment of Active Flow Control, known as AFC, on wings or high-lift devices has again emerged as a solution to the limitations of the shape optimization, limitations of the high lift configuration and environmental issues previously mentioned.

Over the last decade, aerospace organizations such as NASA, DLR, Boeing and the European consortium AFLoNext, have conducted studies on this subject as shown in the works by Bushnell and Wygnanski (2020), Lin *et al.* (2019), Melton *et al.* (2018), Jones *et al.* (2018), Delfs *et al.* (2017), Ciobaca and Wild (2013), DeSalvo *et al.* (2020), Shmilovich *et al.* (2018), Rosenblum *et al.* (2019), Wild (2020) and Hue *et al.* (2017). These authors show that Active Flow Control mechanisms are able to manipulate the fluid flow field from its natural state to a desired state. The injection of high speed jet inside the boundary layer, for example, enables the suppression or delay of the flow separation due to the increase of local momentum and energy of the boundary layer, consequently improving the lift values. An increase of 0.10 in lift coefficient at constant angle of attack may reduce the approach attitude by about one degree, resulting in a weight saving of about 1400 lb due to the shortening of the landing gear. If the increase in maximum lift coefficient reaches 1.5%, the payload may increase 6600 lb at a fixed approach speed. Or, if the lift to drag is increased by 1% on take-off, the payload may increase 2800 lb (Meredith 1993). Moreover, the fuel burn may be reduced by 2.25% with an AFC system applied to a simplified high-lift configuration (Hartwich *et al.* 2017), accompanied by an expected noise and drag reduction, once the slat and flap tracks, and the slots between high lift devices and the main element from conventional systems are eliminated (Delfs *et al.* 2017; Lin *et al.* 2019). Assuming that a wing equipped with an AFC system substitutes a single slotted flap for a hinged plain one, the negative effect of weight additions due to the redundancies of the AFC system is compensated by the benefits of the simplification of the flap system (Hartwich *et al.* 2017). Therefore, a configuration with an AFC system is comparable in weight to a single slotted multi-element one.

At high speeds the Active Flow Control can be applied to advanced nozzles of fighter aircraft in order to provide thrust vectoring and additional propulsive lift with fewer moving parts, resulting in an improvement of around 7-12% of engine thrust to weight ratio (Deere 2003; Anders *et al.* 2004), which emphasizes its importance either for space or military applications. Salimi *et al.* (2022) for example numerically investigated a fluidic thrust-vectoring and achieved a vector angle of 17.1 degrees via slot injection of methane fuel. In cases of transonic flow over wings or airfoils the flow control can act on the moving shock waves downstream, thus expanding the local supersonic zone; suppressing flow separation caused by shock/boundary layer interaction; and delaying the transonic buffeting caused by the pressure fluctuations due to unsteady shock/boundary layer interaction (Abramova *et al.* 2020).

AFC technology had been studied in the past, as can be seen in the works of Lawford and Foster (1969), Dods Jr. and Watson (1976) and Englar and Huson (1983), but the weight penalty caused by the

additional system installation, complexity of the system, and low system efficiency showed that its use would not be feasible, despite the good laboratory results (Washburn *et al*. 2002; Melton *et al*. 2018; Lin *et al*. 2019). However, new mechanisms and methods, such as improvements in computing machinery, computational fluid dynamics and actuators, have changed the approach to flow control. Instead of just adding momentum in the boundary layer region to delay separation, Active Flow Control may utilize instabilities in the flow to augment the control input, as pointed out by Bushnell and Wygnanski (2020), making the cost/benefit ratio even more attractive.

1.2. Active Flow Control

The steady jet can be considered the simplest method of active separation control when applied to a wing or airfoil. In Pavlenko *et al*. (2018) and Petrov (2012), the boundary layer control system employs a tangential compressed air blown over the high-lift devices and control surfaces, supplied from the fan stage or from the high-pressure stage of the engine core of a STOL transport aircraft. The authors also included in their study external blown flaps. By using just the boundary layer control, the jet eliminated the flow separation over the flap with the blowing momentum coefficient, given by Eq. (1), of $C_\mu = 0.03$ at take-off flap position and $C_\mu = 0.04$ at landing position,

$$C_\mu = \dot{m}_j V_j / q_\infty S \qquad (1)$$

where $\dot{m}_j$ is the blowing mass-flow rate, V_j is the jet velocity, q_∞ is the free-stream dynamic pressure and S is the wing reference area. Furthermore, the lift coefficient was shown to increase around 2.5 times when compared to the uncontrolled configuration. In relation to a conventional baseline aircraft, the combined system significantly reduced the fuel consumption by 5%, and the take-off speed by 10%, while landing speed was reduced by 30%. The flight range and payload also increased 10%. The authors also found in a preliminary CFD study that the differential jet was able to compensate for the forces and moments in cases of engine failure, reducing the rolling moment by 37% and yawing moment by 68% at zero sideslip angle during the failure.

Radespiel *et al*. (2016) conducted extensive studies on steady tangential and oblique jets on the transonic airfoil DLR-F15 equipped with a plain flap. The tangential jet showed enhancements of 2 to 5 in lift coefficient, which makes its employment very interesting for STOL applications.

In contrast to the steady blowing jets that re-energize the boundary layer, the principle behind unsteady jets (oscillatory) is to generate boundary layer instabilities. The introduction of oscillations inside the boundary layer flow at specific frequencies enhances its high momentum, and as a result, the flow withstands larger adverse pressure gradients without separating. The effect of this process of generating instabilities is compared to the existence of large turbulent coherent structures, which increase the entrainment by means of turbulent momentum transport (Seifert *et al*. 1993, 1996), and consequently increases lift. Therefore, the use of oscillatory jets to control the boundary layer separation improves the generation of vortices, that periodically transfer streamwise momentum from the outer flow to the surface (Greenblatt *et al*. 2010), enhancing the capability to maintain the boundary layer attached at larger adverse pressure gradients. In terms of aerodynamic improvement, the unsteady jet devices can perform equally well or, in some cases, present superior control performance when compared to the steady jet, with the advantage of requiring a reduced mass blowing rate from the system. Recent studies, which also combine continuous and oscillatory jets as carried out by Seifert *et al*. (1993), were performed by Singh *et al*. (2021). Instead of supplying the hybrid jet to the flap region, the research was based on the jet application to the leading edge (12% *c*), where a significant stall delay was observed, changing the angle of stall from 16° to 20° when the mean velocity of the hybrid jet was equal to the free stream.

In order to obtain aerodynamic improvements using unsteady jets, besides the slot geometry optimization, jet parameters also have to be optimized. In an AFC system, it is possible to define two regimes, namely, boundary layer control and super-circulation. The boundary layer control acts in the range from the delay of the separation somewhere on the flap up to its suppression. The lift aerodynamic force increases as the blowing momentum coefficient, C_μ, increases. The detachment suppression occurring in the boundary layer control regime leads to a fast lift increase. When the flow is completely attached to the surface, the so-called super-circulation begins. For this regime, the lift also increases when the C_μ parameter increases, however, the greater the blowing momentum coefficient the slower the gain of lift, thereby demanding more energy from the system. Thus, the most efficient operation of separation control is the limit point between boundary layer control and super-circulation (Radespiel *et al*. 2016). According to Jones *et al*. (2006), this point is based on the change in lift efficiency as a function of C_μ, whose value is difficult to predict. As the physical phenomenon of the transition from one regime to the other is related to the end of flow separation, Particle Image Velocimetry experiments, PIV, or CFD simulations, can help to obtain this transition point.

For unsteady jets, the jet frequency is another variable to be analyzed, which is more typically used in AFC systems as reduced frequency F^+, given by

$$F^+ = f x_{TE} / V_\infty \qquad (2)$$

where f is the jet frequency, x_{TE} is the distance from the actuators to the trailing edge and V_∞ is the free stream velocity. Several works exploited the variation of the reduced frequency (Seifert *et al*. 1993, 1996; Liu *et al*. 2004, 2020). The main conclusion was that the optimum performance is obtained with $F^+ = 1$, as shown by Seifert *et al*. (1996). However, Liu *et al*. (2004) also showed that the most efficient frequency can be achieved using

higher frequency, $F^+ = 2.82$, which corroborates with the idea that the optimum frequency may be dependent on each specific configuration.

Pulsed jets generally work by employing fast-acting solenoid valves, high-speed rotating valves, or piezoelectric actuators. The advantage of this system is the possibility of achieving high-speed jet flow, as demonstrated by Hogue *et al.* (2009), where a Mach number of 1.5 was obtained using a piezoelectric actuator coupled to a convergent-divergent micro nozzle. However, while pulsed jet systems can supply higher flow speeds, they are always limited due to their dependence on external sources.

Two waveforms can be used to model pulsed jet applications, namely, sinusoidal or square. Pulsed jet by means of sinusoidal function was studied by Ekaterinaris (2004). The author applied pulsed jet to the leading edge of a modified NACA0015 airfoil and analyzed the effect of the reduced frequency F^+ and sinusoidal jet exit velocity on the behavior of the lift coefficient, C_L, close to and after the stall region. Up to stall, higher F^+ reduced the amplitude oscillation of the lift coefficient and favored the increase of C_L average value. After the stall, the beneficial effect of increasing the average C_L comes from the increase in jet velocity; however, an increase in the amplitude oscillation is observed. Liu *et al.* (2004) conducted research based on numerical analysis of a circulation control wing equipped with both a steady and a pulsed jet with square waveform at the leading edge. Maintaining the airfoil chord and free-stream velocity constant, the authors observed that the lift coefficient varied from 1.58 to 1.80 when the reduced frequency changed from $F^+ = 0.7$ ($f = 100$ Hz) to $F^+ = 2.8$ ($f = 400$ Hz). They also concluded that for higher frequencies the pulsed jet required a lower mass flow rate than a steady jet. For example, when $f = 400$ Hz, the pulsed jet required 73% of the steady jet mass flow rate and the average lift achieved 95% of that found with a steady jet control system. Haucke and Nitsche (2013) used a square wave voltage to control fast solenoid valves as separation control in the DLR F15 airfoil. The wind tunnel tests showed that the application of the jets to the trailing edge flap by the actuator rows increased the lift coefficient by 0.7 at a frequency of 100 Hz when compared to the baseline case.

Synthetic jets are another form of flow control within unsteady jet applications. They are typically known as zero-net mass flux, ZNMF. The negative/positive portions of the wave signal represent suction/blowing. The synthetic jet actuators, SJA, are generally piezoelectric sensors, where the diaphragm oscillates around the equilibrium state, thus generating suction and blowing. The synthetic jet was shown to be very effective for separation control and can be applied to the slat or the flap. Besides the good results obtained when the synthetic jet is applied to aerodynamic shapes, another advantage is that this system does not require an external fluid source. On the other hand, actuators used for ZNMF have the disadvantage of peak jet velocities limited to moderate subsonic speeds (Cattafesta and Sheplak 2011), around 100 m/s, that may not be feasible for realistic aircraft applications (Rosenblum *et al.*

2019). Moreover, actuators must be operated near the mechanical resonance for satisfactory performance, which can lead to mechanical failure of the device (Tesar *et al.* 2006). An analysis performed by Chapin and Bernard (2015), focusing on synthetic jets applied to the NACA 0012 airfoil, found quite similar results in C_{Lmax} and angle of stall when comparing pulsed and synthetic jets. Additionally, synthetic jets have shown low applicability in high adverse pressure gradients, for example, at high angle of flap deployment. A concern regarding synthetic jets was stated by Melton *et al.* (2018), where the unsteady excitation produced by synthetic jets or sweeping jet actuators were unable to reattach the separated flow with flap deflected up to 60°.

1.3. Objective of this Paper

Various references, such as those presented in sections 1.1 and 1.2, used separation control on different systems, on different aerodynamic shapes and locations, which increases the difficulty of comparisons between the published results. Even considering the same basic flow field, different effects can be found due to the variety of systems and geometries, as cited by Greenblatt *et al.* (2010). Therefore, the main objective of this paper is to evaluate different separation control systems by tangential jets applied to the flap shoulder of a high lift configuration, using the mechanisms of steady, pulsed and synthetic jets control, with variations on the intensity of jets, slot height, frequency and leading edges, considering modifications for the same baseline wing. This initial analysis serves as a benchmark to study the feasibility of the substitution of a conventional single slotted high-lift configuration to one equipped with separation control.

2. COMPUTATIONAL GEOMETRIES AND METHODS

2.1. Baseline Model

The baseline geometry adopted here is the aerodynamic model studied in the first AIAA CFD High Lift Prediction Workshop (HiLiftPW-1), the NASA Trapezoidal Wing (Rumsey *et al.* 2011, Slotnick *et al.* 2011). It consists of a four part body composed of the main wing, full-span slat, full-span flap and body pod. The model is a simplified high-lift geometry, untwisted, with no dihedral, three-element semispan swept wing attached to the body pod. It is equipped with a movable leading edge slat and Fowler flap, where gaps (slots) are formed when the slat and flap are deflected.

Two configurations were presented in the AIAA workshop and configuration 1 (leading edge slat deflected 30°, flap deflected 25°) was chosen to be studied here. Even though the model is a simplified geometry, the flow presents the same complex phenomena found in high lift systems of a typical aircraft, such as laminar flow, laminar/turbulent transition, relaminarization, transonic slat flow,

(a) Upper view.　　　(b) Lower view.
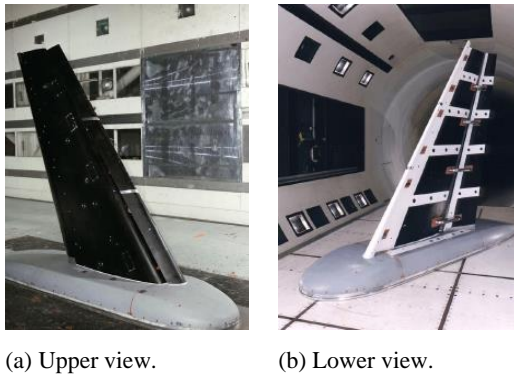
Fig. 1. NASA Trapezoidal Wing installed at NASA Langley 14x22ft Wind Tunnel (Crippa *et al.* 2011).

confluent boundary layers, wake interactions, separation and flow reattachment, streamline curvatures and possible unsteady flow (Meredith 1993; Johnson *et al.* 2000; Rumsey *et al.* 2011; Hannon *et al.* 2012). The reference wing chord is 1.006 m based on the stowed configuration (cruise). Figure 1 shows the wing model installed in the NASA Langley 14x22ft wind tunnel.

2.2. Modified Model

New configurations were created based on configuration 1 of the original NASA Trapezoidal Wing model. The modifications were based on changes of the Fowler flap to plain flap, slat configurations, and the generation of the slot formed between the main wing trailing edge and the flap. In order to create the new geometries, the flap was positioned at the cruise configuration, given by the transformation from the unstowed to stowed conditions (Rumsey and Hannon 2011) and the flap was rotated 25° around the hinge point, located at the quarter-chord of the flap. After the flap rotation, a slot with a height of 0.085% of the chord *c* was generated. To finalize the model modifications, the lower surface was extended to the hinge point, removing the original gap between the lower surface wing and flap. Figure 2 shows the details of the flap modification. The procedure was repeated to create the configuration with a flap deflected 50°. Minor corrections were made to maintain the same flap geometry and slot height along the wing length.
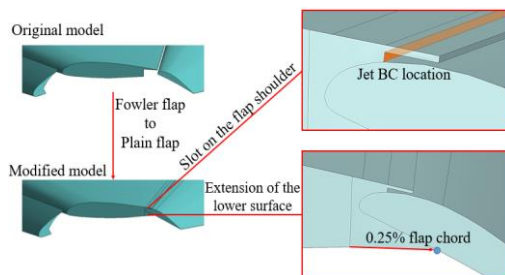
Fig. 2. Detail of the flap modifications.

According to Radespiel *et al.* (2016), research on leading edge for Coanda flaps is rare. Their work showed that the gapped slat could not effectively contribute to the increase in performance as expected in cases of blowing. Moreover, Englar (1972) associated the increase in lift with the movement of the leading edge stagnation point, increase in effective camber and circulation around the airfoil. Therefore, different leading edge configurations were investigated in this present work to check the influence under the blowing system, clean (without slat), cruise (stowed), baseline configuration (leading edge slat) and droopnose. The droopnose was constructed from the stowed position, and rotated 30°. The translation of the slat was performed in such a way that the upper surfaces of the main wing and slat became coincident. Figure 3 shows the baseline configuration, and the five proposed modifications for the simulations with Active Flow Control.
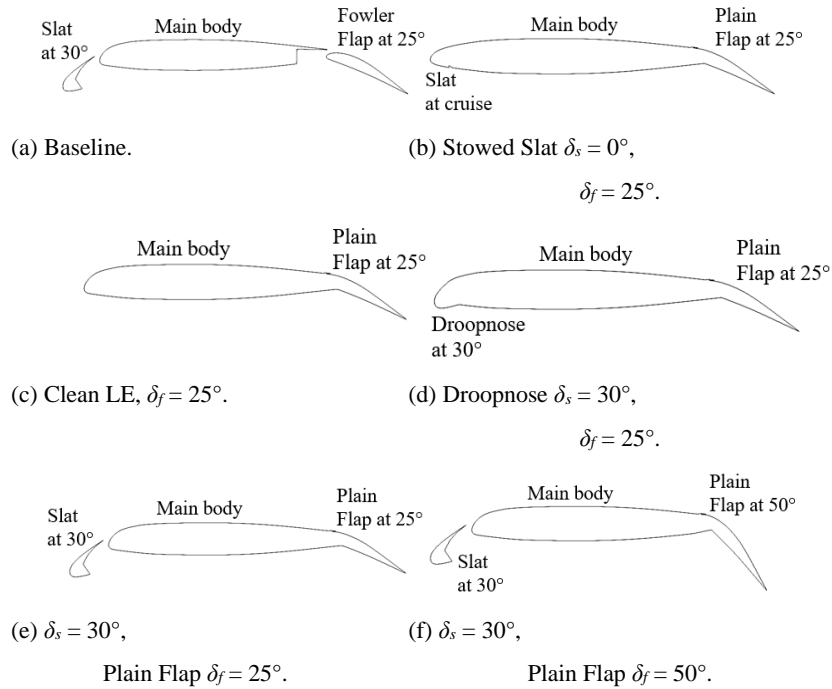
The computation of the lift and drag coefficients requires information regarding the resultant forces, which are summed from the slat, main wing and flap, along with the free stream conditions and the geometry of the multi-element airfoil. Concerning the geometry, the configurations namely Baseline (Fig. 3a), Stowed Slat (Fig. 3b), Plain Flap at 25° (Fig. 3e) and Plain Flap at 50° (Fig. 3f) consider the same reference chord, which is based on cruise configuration of 1.006 m, since the modified plain flaps were placed at cruise position and they use the same slat. The configurations Clean Leading Edge (Fig. 3c) and Droopnose (Fig. 3d), where the slat is not considered or modified, have their lengths discounted from the baseline wing reference chord accordingly.

The present research analyzes only the effectiveness of flow control applied to the flap region. Some works such as Chapin and Bernard (2015), Durrani and Haider (2011) and Ekaterinaris (2004) applied flow control to the leading edge instead of to the trailing edge. The aerodynamic improvement obtained is mainly due to the stall delay with a slight gain in lift coefficient in comparison to the no control configuration. It was observed that only a strong jet on the leading edge was able to overcome the adverse pressure gradient at high angle of attack. According to Seifert *et al.* (1996), the quadruple of the blowing momentum coefficient on the leading edge is required for the same lift encountered by the flap jet, in both steady and unsteady jets.

2.3. Computational Set-Up

The SU2 code was used to obtain the numerical results presented in this research. The SU2 code is an open source finite-volume RANS/URANS solver capable of simulating compressible and turbulent flows, which can perform aerodynamic shape optimization (Palacios *et al.* 2014).

The simulations presented here are based on the steady and unsteady Reynolds-Averaged Navier-Stokes equations (RANS/URANS), in a two-dimensional domain. Initially, the Spalart-Allmaras, SA (Spalart and Allmaras 1992), and Menter's Shear Stress Transport, SST (Menter 1994), turbulence

(a) Baseline.

(b) Stowed Slat $\delta_s = 0°$,

$\delta_f = 25°$.

(c) Clean LE, $\delta_f = 25°$.

(d) Droopnose $\delta_s = 30°$,

$\delta_f = 25°$.

(e) $\delta_s = 30°$,

Plain Flap $\delta_f = 25°$.

(f) $\delta_s = 30°$,

Plain Flap $\delta_f = 50°$.

Fig. 3. NASA Trapezoidal Wing profiles, baseline and modified configurations used in the present study.

models were chosen as closure models. After a validation study conducted with available wind tunnel data of the RAE 102 airfoil with steady jet applied to the flap shoulder, the SST turbulence model supplied better results and was adopted for the simulations.

The SU2 discretization scheme is based on the method of finite volumes in unstructured meshes. Roe's second-order upwind scheme was used to calculate the convective fluxes and the linear system is solved using the iterative FGMRES (Flexible Generalized Minimum Residual) method. The Lower-Upper Symmetric Gauss-Seidel linear pre-conditioner was used to accelerate the convergence. The convergence criterion was set to a residual value of 1×10^{-6} of the integrated quantity C_L. When the convergence criterion is reached the simulation is stopped. For unsteady flow (URANS), an implicit dual-time-stepping strategy was used to achieve high-order accuracy in time, where the unsteady problem is transformed into a series of steady problems at each physical time step which can be solved consecutively (Economon *et al.* 2016). The convergence criterion used for unsteady flow is different. The number of iterations in each dual-time-stepping is constant and chosen according to a parametric analysis, as will be explained further in greater detail in section 4.2. The simulation is stopped manually when the results present a steady behavior, *i.e.*, the C_L response is repeated during the cycles, which usually occurred after approximately 80 actuation cycles. Other authors such as Shmilovich *et al.* (2018), found a convergence cycle after around 50 actuation cycles. In order to reduce the computational cost of unsteady cases, steady-state solutions were used as initial conditions. The

job processes were solved in parallel in a computer cluster consisting of PC blades of Intel Xeon E5-2680 with 10 and 14 cores.

2.4. Boundary Conditions

Although the jet boundary conditions are specific for each case, the outer domain and the wall surfaces are the same for all simulations. The farfield conditions were applied as Mach number 0.2, the desired flow angle of attack and free-stream temperature of 288.9 K, based on the characteristic variables employing Riemann invariants. The airfoil surfaces use the adiabatic and no-slip conditions.

In the case where a steady jet was employed, the simulation was performed as steady state, with the jet boundary condition set as subsonic inflow. In order to set this inlet condition, the TOTAL_CONDITION SU2 command was used, constituted by location, total temperature, total pressure and flow direction vector, where the total temperature is set to be equal to the total free-stream temperature and the total pressure is imposed to a desired value. The inlet boundary condition already exists in the SU2 code and it is only necessary to set the correct value of total pressure to achieve the required C_μ, calculated by Eq. (3) for two-dimensional cases, which is a simplification of Eq. (1) considering full span slot,

$$C_\mu = \rho_j V_j^2 h / q_\infty c \qquad (3)$$

where ρ_j is the jet density, h is the slot height and c is the wing chord. For the unsteady cases, the blowing momentum coefficient is counted during each physical time step, where the total C_μ value is the sum of all portions of the signal period.

Although the SU2 code is a continuously updated open source one, no time-dependent boundary conditions have been implemented to date in the SU2 suite for this specific simulation. Two signal types of pulsed jet are studied in this research: sinusoidal and square wave with a duty cycle of 50%. The boundary conditions at the plenum chamber outlet vary in accordance with the jet configuration. Thus, for the time dependent jets, new implementations in the source codes were necessary. To correlate the input signals with the real actuation of the separation control devices, a high-speed rotating valve operation can be represented by a sinusoidal signal while a fast-acting solenoid valve operation can be represented by a square wave signal. The equations in terms of total pressure used for sinusoidal and square wave jets are represented by Eqs. 4 and 7, respectively,

$$P_0(t) = A\sin(\omega t) + B \qquad (4)$$

$$A = (P_{0,peak} - P_{0,OFF})/2 \qquad (5)$$

$$B = (P_{0,peak} + P_{0,OFF})/2 \qquad (6)$$

where $P_{0,peak}$ is the maximum total pressure, $\omega = 2\pi f$ is the angular frequency of the unsteady jet, $P_{0,OFF}$ is the total pressure when the velocity at the slot is null and t is the physical time step. When a square wave jet is set, the following conditional statement is imposed in order to apply the maximum or the minimum pressure (no control).

$$\text{if } (P_0(t) > = B \ \{P_0(t) = P_{0,peak}\}$$
$$\text{else } \{P_0(t) = P_{0,OFF}\} \qquad (7)$$

In the case of synthetic jets where two different natures of boundary conditions must be established, a logical statement was added into the code to lead to the type of boundary condition (inlet or outlet), promoting suction or blowing depending on the physical time step. In general, the synthetic jets are generated from piezoelectric actuators formed by diaphragm oscillators and driven by a sinusoidal signal. Some authors such as Durrani and Haider (2011) and Liu *et al.* (2020) modeled the synthetic actuators with moving grids to simulate the vibration of the diaphragm motion, while Holl *et al.* (2012) and Chapin and Bernard (2015) imposed the velocity profile generated from generic actuators. In this research, we used the second option, *i.e.*, the meshes were kept constant and equations were used to simulate the airflow perturbations. The equation for pure sine jet application is shown in Eq. 8. For the synthetic jet, the P_0 mean value is equal to $P_{0,OFF}$ and corresponds to the null velocity at the slot.

$$P_0(t) = 2A\sin(\omega t) + P_{0,OFF} \qquad (8)$$

Figure 4 shows the generated signal jets for each configuration, and Fig. 5 shows a general scheme for the unsteady boundary conditions explained in this section.
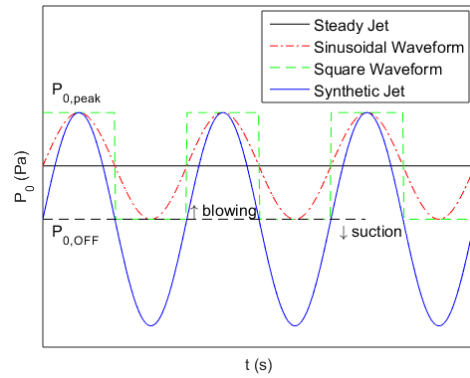
**Fig. 4. Examples of Steady, Pulsed and Synthetic jet signals.**
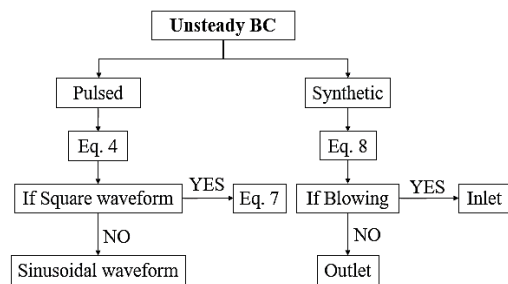
Fig. 5. Scheme of Unsteady boundary conditions.

3. VALIDATION

The effectiveness of CFD tools to study Active Flow Control and to represent the actual flow depends on the choice of numerical methods, turbulence models, boundary conditions and grid generation. This section presents the validation of the SU2 code for the RAE 102 airfoil, with tangential steady jet at flap deflected 20°, $M = 0.131$ and $Re = 3.78 \times 10^6$. The wing thickness ratio is 0.13, and cambered for a design lift coefficient of 0.2. The plain flap is 25% of chord, which is hinged on the lower surface. The jet was applied tangentially to the main body upstream of the flap, with the nozzle height of the jet being 1.0668×10^{-3} m (0.042 in). The plenum chamber was created in order to supply the required outlet slot condition and simulate the jet on the airfoil. More details can be viewed in Goffert *et al.* (2021).

Curves for the lift coefficient, C_L, versus angle of attack, α, for the RAE 102 airfoil are presented in Fig. 6. Figure 6a shows the $C_{L\alpha}$ distribution for both the no blowing condition and undeployed flap. Note that the numerical results agree very well with the experimental data (Lawford and Foster 1969) in the linear region for both turbulence models, SA and SST. The SU2 results overestimated C_L near the stall region and both turbulence models calculated the stall at 17°, while the wind tunnel experiment predicted the stall at 16°. The stall type in the wind tunnel experiment may be associated with laminar separation at the beginning of the wing section, which results in an abrupt drop of lift, as can be seen in the experimental data of Fig. 6a. As the RANS code used in the present research considers fully

(a) Base airfoil. (b) $\delta_f = 20°$, $C_\mu = 0.008$. (c) $\delta_f = 20°$, $C_\mu = 0.047$.
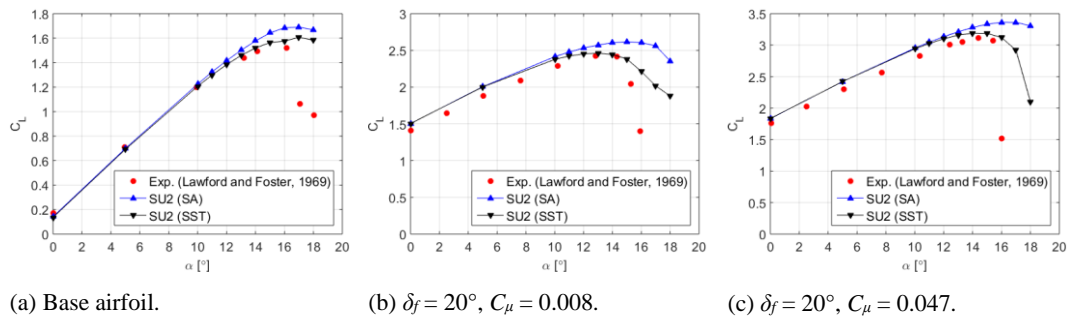
Fig. 6. RAE 102 airfoil, distribution of C_L x α.

turbulent flow without transition modelling, the turbulent boundary layer at the leading edge can withstand larger adverse pressure gradients without separation. The lack of precision in stall prediction is not unusual when using RANS codes, as can be seen for example in Rumsey *et al.* (1997), where they also found differences in stall characteristics of the high-lift AGARD model.

Figures 6b and 6c present the curves C_L versus α for the deployed flap at 20° and blowing with $C_\mu = 0.008$ and $C_\mu = 0.047$, respectively. In general, the lift coefficient was over predicted when compared with experimental data with differences of C_L around 0.1. Provided that the grid resolution accurately resolves the suction peak, the linear portion of the lift curve is not affected by the different turbulence models. However, when non-linear effects become relevant, as in the near stall region, the use of different turbulence models provides widely different values for the aerodynamic coefficients.

The C_L curves are close to the experimental data for both turbulence models in the linear region, but the SST performance is superior close to the stall region, which motivated its use in the present study.

4. MESH GENERATION

After the geometry preparation, the 2-D meshes were generated. Unstructured hybrid meshes were created using an extrusion process combined with the Delaunay triangulation mesh. This method combines quadrilateral elements in the boundary layer region and triangular elements in the rest of the 2-D mesh.

The generated meshes are type O-meshes, with a farfield frontier which is 100 times the value of the wing reference chord distant from the geometrical center of the airfoil. Although $k\text{-}\omega$ model, which is part of Menter's SST formulation, can be run with the first grid point as far as $y^+ = 3$ without deterioration of the results (Menter 1994), the first layer spacing was initially set to $y^+ = 1$, satisfying $y^+ \leq 3$ after running over the whole wing section. Local refinements in the leading edge were performed to reduce sharp edges and to resolve the high gradients properly. The growth rate normal to the viscous region was kept at 1.08, where 80 quad layers were created, and a growth rate of 1.2 in the outer flow was used for the triangular elements.

The mesh topology is similar to the generated mesh for the validation cases. Figure 7 shows an example of the mesh close to the wing section for the modified model with $\delta_s = 30°$ and $\delta_f = 25°$, and a detail of the AFC duct.
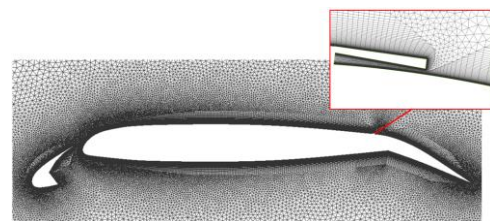
Fig. 7. Example of the medium mesh with detail in the separation control region, $\delta_s = 30°$, $\delta_f = 25°$.

The domain of each mesh configuration used in the simulations is detailed in Table 1, where the total element type, first element height and the average y^+ over the airfoil are shown. The IDs represent the configurations: Baseline (1); Stowed Slat $\delta_s = 0°$ with Plain flap $\delta_f = 25°$ (2); Clean LE with Plain flap $\delta_f = 25°$ (3); Droopnose $\delta_s = 30°$ with Plain flap $\delta_f = 25°$ (4); Modified with Slat $\delta_s = 30°$ and Plain flap $\delta_f = 25°$ (5); and Modified with Slat $\delta_s = 30°$ and Plain flap $\delta_f = 50°$ (6), as can be seen in Fig. 3.

Table 1 Mesh parameters of the medium meshes.

ID	Triangular	Quad	First element height (m)	Avg y^+
1	66,077	77,451	6×10^{-6}	1.02
2	70,221	72,440	6×10^{-6}	0.85
3	66,152	62,010	6×10^{-6}	1.00
4	62,494	66,620	6×10^{-6}	0.92
5	72,442	77,541	6×10^{-6}	0.95
6	68,888	80,390	6×10^{-6}	0.84

The evaluation of the mesh quality was based on three element metrics: skewness, maximum included angle and area ratio. Table 2 shows the total elements of each mesh, and the quantity of elements according to the presented metrics. According to the data provided by the table, less than 0.2% of the elements are above 0.8 of skewness, less than 0.3% of the elements presented an angle higher than 120°, and

Table 2 Quality of the medium meshes.

ID	Total elements	Skewness < 0.8	Angle < 120°	Area Ratio < 5
1	143,528	143,366	143,294	142,565
2	142,661	142,404	142,250	142,183
3	128,162	128,057	128,035	127,924
4	129,114	129,003	129,032	128,882
5	149,983	149,846	149,709	149,520
6	149,278	149,141	149,002	148,849

less than 0.7% of the elements presented an aspect ratio higher than 5. In case of aspect ratio, the elements with higher values are the elongated quad elements close to the surface. They present low height in comparison to the length, which is acceptable once the higher gradients are found perpendicular to the wall and not aligned to the flow.

4.1. Mesh Sensitivity Study

Four additional meshes were generated to check the sensitivity of the code according to the grid refinement. Two of the finest meshes and two of the coarsest meshes were derived from the medium mesh described in section 3.4, respecting the element duplication or halving process for the quadrilateral elements close to the boundary layer region. Outside this region, the growth rate was also adjusted linearly to create some refinement procedure.

It is well-known that for unstructured meshes, refinement analysis can be hard to perform due to difficulties of merging or dividing elements in a manner that preserves the element type while enforcing the grid refinement factor over the domain (Oberkampf and Roy 2010). Therefore, the methodology employed here attempts to create an approach which is as close as possible to that used in structured grids. The cases selected to evaluate the mesh sensitivity, shown in Table 3, are based on high C_L values, with the presence of flow separation and close to stall. Free-stream conditions of $M = 0.2$ and $Re = 4.3 \times 10^6$ and no separation control were considered in this analysis.

Table 3 Cases for mesh sensitivity study.

ID	Configuration	α (°)
1	Baseline	20
2	Stowed slat, $\delta_f = 25°$	10
3	Clean LE, $\delta_f = 25°$	10
4	Droop $\delta_s = 30°$, $\delta_f = 25°$	10
5	$\delta_s = 30°$, $\delta_f = 25°$	20
6	$\delta_s = 30°$, $\delta_f = 50°$	20

Figure 8 shows the evolution of the lift coefficient with the increase of mesh refinement. It is clear that the medium mesh for the baseline, clean configuration, droopnose and slat at cruise position already converged, *i.e.*, the results are independent of the mesh refinement. For modified configurations with the original slat deflected at $\delta_s = 30°$, the lift

coefficient of the finest meshes presented a slight reduction of 1.4% and 1.1% in relation to the medium meshes for $\delta_f = 25°$ and $\delta_f = 50°$, respectively. As the finest meshes are considered to be converged, when the grid convergence index, GCI, calculated according to Celik *et al.* (2008), is below 0.3% for these configurations, the medium meshes may be accepted since this condition near the stall is very critical due to the turbulent motion. It is worth mentioning that these medium meshes will also be used for the unsteady cases, where the quality of results must be balanced with the computational cost.
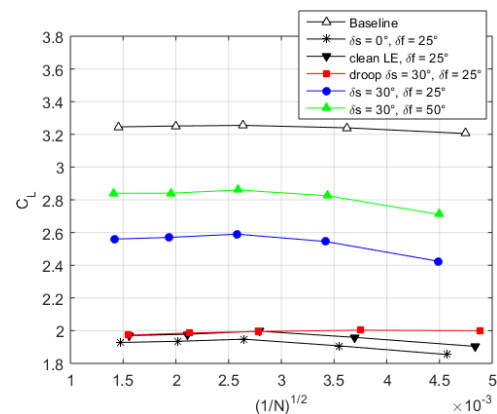

Fig. 8. Mesh sensitivity of the lift coefficient.

5. RESULTS AND DISCUSSION

The results obtained by the numerical simulations are divided in two subsections: Steady Jet, where the influence of the proposed leading edge configurations, intensity of blowing and slot height over the lift coefficient employing steady jet were investigated; and Unsteady Jet, where results from the analysis of synthetic and pulsed jets with sinusoidal and square waveforms, variations of frequency and mass flow used in each system were studied. Both flap deflections of $\delta_f = 25°$ and $\delta_f = 50°$ were evaluated in the subsections. The free-stream conditions for all simulations were set for $M = 0.2$ and $Re = 4.3 \times 10^6$.

5.1. Steady Jet

The effects of variation of the blowing momentum coefficient, C_μ, on the lift coefficient, C_L, were investigated for the modified geometries. Figures 9-11 show the lift coefficient curves as a function of the angle of attack for the modified versions. The results of the original NASA Trapezoidal Wing section, presented in Fig. 3a, with slat deflected 30° and Fowler flap at 25° are also included in the figures as a 'Baseline' reference. Regarding the modified geometries, all configurations with no jet blowing presented stall behavior with a rapid drop of lift. We expected a higher lift for the stowed slat (Fig. 9a) than for the clean configuration (Fig. 9b) due to the increment of the chord length, but the presence of the slat at cruise position showed neither benefits in C_L nor delay of stall. In fact, the slat at cruise

(a) Stowed slat, $\delta_f = 25°$.

(b) Clean LE, $\delta_f = 25°$.

(c) Droopnose $\delta_s = 30°$, $\delta_f = 25°$.
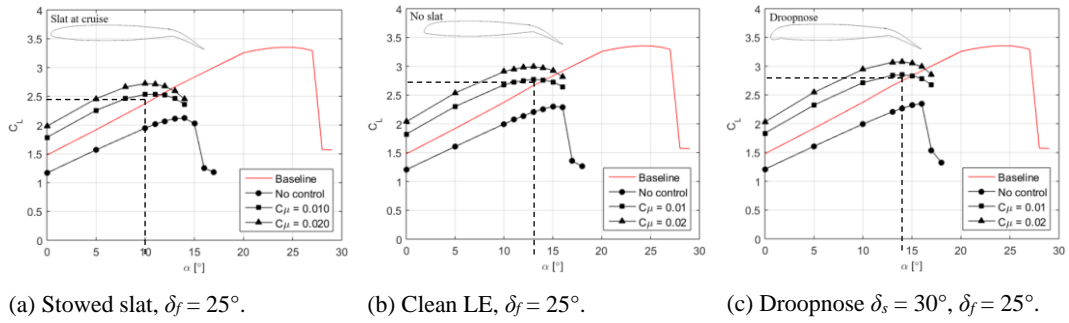
Fig. 9. C_L x α for modified and baseline configuration.

configuration (stowed) presented a lower C_{Lmax} and a lower angle of stall (Fig. 9a). As can be seen in Fig. 9c, the droopnose improvement in C_{Lmax} is slightly better than the clean configuration, and the angle of stall is postponed from 13° to 14°. Apparently, the generated droopnose was not sufficient to cause significant flow changes, even with a deflection δ_s equal to 30°. However, a more protuberant droopnose can be effective, as shown in Radespiel *et al.* (2016) and Kauth *et al.* (2017). Geometries with modified leading edges (Figs. 3b, 3c and 3d) do not seem to be suitable configurations due to the very early stall, between 10° and 14°, and low C_{Lmax} with moderate jet.

Figures 10 and 11 show the results for the configurations with the baseline leading edge slat, $\delta_s = 30°$, and plain flaps deflected 25° and 50°. It can be noted that the baseline C_{Lmax} was achieved with jets of $C_\mu = 0.010$ and 0.005 for the plain flap configured at 25° and 50°, respectively. The angle of stall remained the same as the baseline in all conditions studied for $\delta_f = 25°$. Regarding $\delta_f = 50°$, the angle of stall dropped from 25° to 22° with $C_\mu = 0.005$ and decreased consecutively with the increase of blowing. According to the results found, the modified geometries which maintain the original baseline leading edge slat, $\delta_s = 30°$, presented the most adequate configurations for a typical aircraft. Consequently, the subsequent investigations with jet variations will be based only on these two configurations, *i.e.*, original baseline slat at $\delta_s = 30°$ combined with modified flap at $\delta_f = 25°$ and $\delta_f = 50°$ (Figs. 3d and 3e).
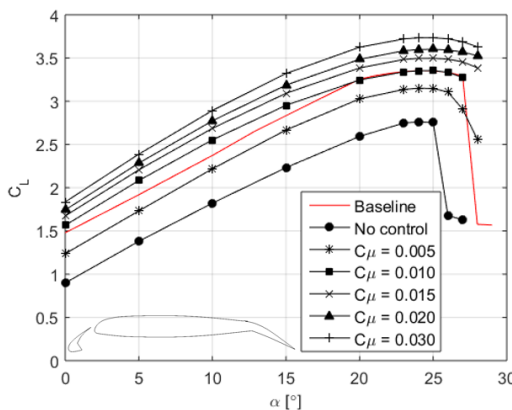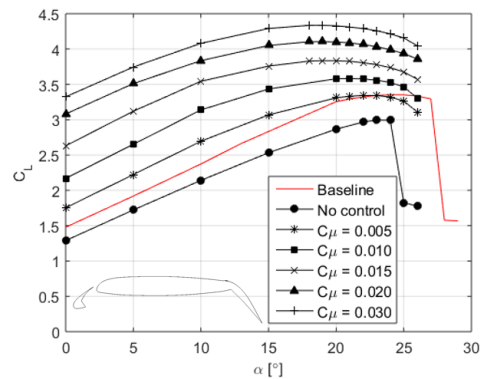
Fig. 11. C_L x α, $\delta_s = 30°$ and $\delta_f = 50°$.

Pressure coefficient distributions, C_p, for the baseline model and modified models with $\delta_f = 25°$ and $\delta_f = 50°$ are shown in Fig. 12. The selected angles of attack were based on the maximum C_L shown in Figs. 10 and 11. Because of the geometry modifications, when the flow control is not applied, the slat (Fig. 12a) and main wing (Fig. 12b) curves presented the lowest suction peaks, and constant values at the flap (Fig. 12c) due to the separated flow. As the AFC is applied and increased, the tendency of the curves is to present higher suction peaks followed with the shift of the curves induced by the increase of momentum downstream of the flap, which results in an increase in C_L. It is well known that the separation control at the flap shoulder impacts the flow around the whole airfoil, but it is still interesting to observe how much the slat was influenced by the AFC application, with an increase of the suction peak up to 65%. It is important to explain that the jump observed after the suction peak at the main element in all cases is due to the geometry curvature that receives the slat trailing edge at the stowed position and not a physical phenomenon resulting from the flow control. Regarding the pressure distribution on the flap, for better understanding the baseline reference was shifted to the same trailing edge point of the modified configuration (Fig. 12c). With $C_\mu = 0.010$, similar levels of C_p such as those of the baseline were achieved, corroborating with the correspondence between the maximum C_{Lmax} values at $\alpha = 25°$, as shown in Fig. 10. With the increase in the blowing, the C_p becomes lower and even more pronounced when the flap is deflected at 50°, which explains the highest lift coefficient values observed in Fig. 11.

Fig. 10. C_L x α, $\delta_s = 30°$ and $\delta_f = 25°$.
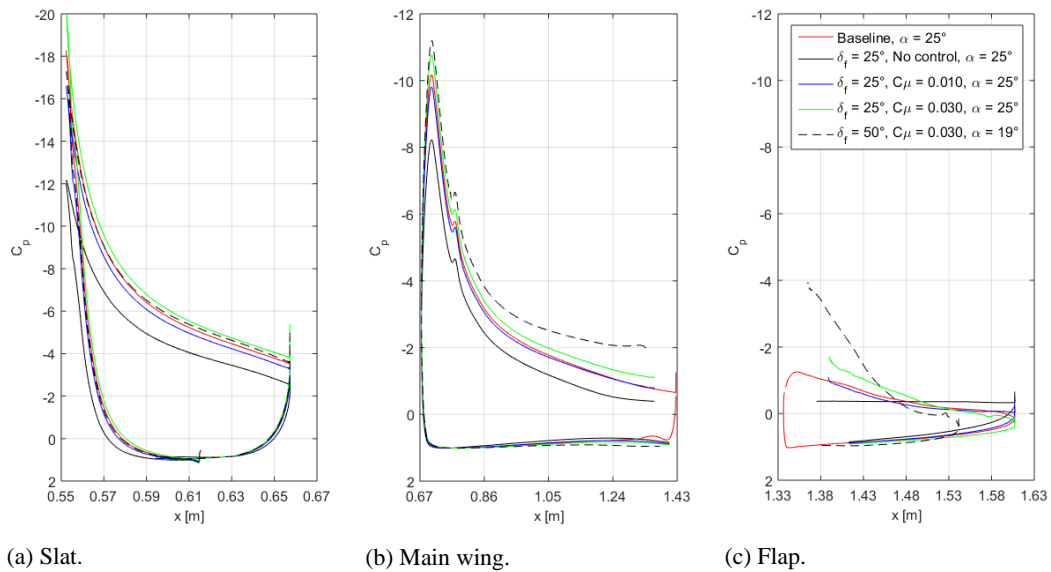
(a) Slat. (b) Main wing. (c) Flap.

Fig. 12. Comparison of pressure coefficient distribution, original leading edge with plain flap and baseline flap configurations.

After choosing the geometries, the efficiency of the proposed jets on the modified model was studied. Figure 13 shows the aerodynamic loads for steady jets in terms of lift-to-drag versus angle of attack (Fig. 13a) and versus lift coefficient (Fig. 13b). According to the figures the high effectiveness is related to low values of angle of attack and low flap deflection. For the least deployed flap the efficiency decays after $\alpha = 10°$ and for the most deployed flap the maximum efficiency is achieved at null angle of attack, with exception for low blowing momentum. At high angles of attack, where the maximum lift is obtained, the values of lift-to-drag are almost constant with the increase in blowing momentum, and consequently with the increase in lift, for both flap deflections, as can be seen in Fig. 13b.

Figure 14 shows the curves C_{Lmax} versus C_μ. A small amount of jet application implies a quick increase in lift as separation is delayed. As can be seen, with a C_μ of only 0.0025 the increase in lift is 0.25 while with a C_μ of 0.01 the increase is 0.6. Simulations at the stall angle of attack were performed varying C_μ to achieve the super-circulation regime, where the flow is completely attached. The limit between boundary layer control and super-circulation is the optimum AFC efficiency and is indicated in Fig. 14, which occurs with $C_\mu = 0.011$ and 0.022, for flap at 25° and 50°, respectively. From the super-circulation regime on, the addition of lift demands a higher quantity of mass flow and pressure supplied by the separation control system. The C_{Lmax} found for the maximum C_μ is 3.734 for flap at 25° and 4.336 for 50°, against 3.352 obtained for the baseline configuration. Therefore, the lift gains related to the baseline configurations are around 11.4% and 29.4%, respectively.

Figure 15 illustrates the benefits of the AFC applied to the flap shoulder. The streamlines and pressure coefficient contours around the models with no control (Figs. 15a and 15c) and at the limit between
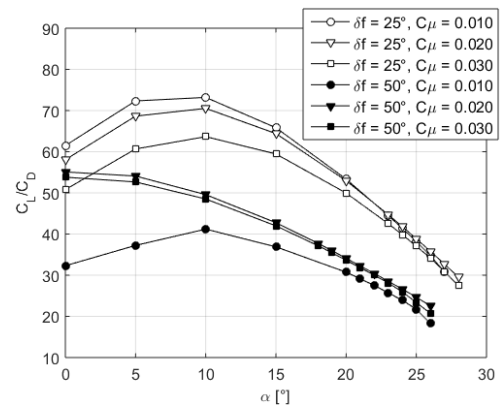
(a) Lift-to-drag x α.
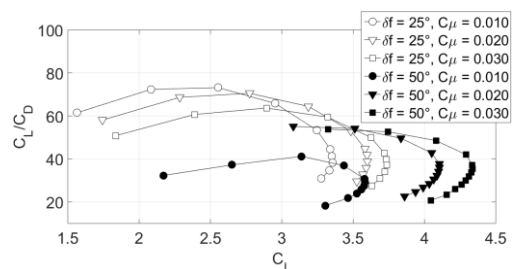
(b) Lift-to-drag x C_L.

Fig. 13. Aerodynamic efficiency (C_L/C_D) for Steady jets.

boundary layer control and super-circulation regime (Figs. 15b and 15d), are shown. The AFC application favors the flow attachment even at the highly deflected angle of flap equal to 50°. There is an increase in low pressure on the upper surface and an increase in high pressure on the lower surface, resulting in a gain in lift. Even though the separation is suppressed in both configurations, some small flow perturbations downstream of the flap still remain. This behavior does not mischaracterize the start of the super-circulation regime, as the flow is
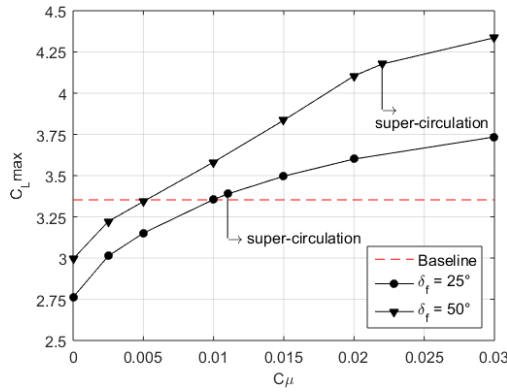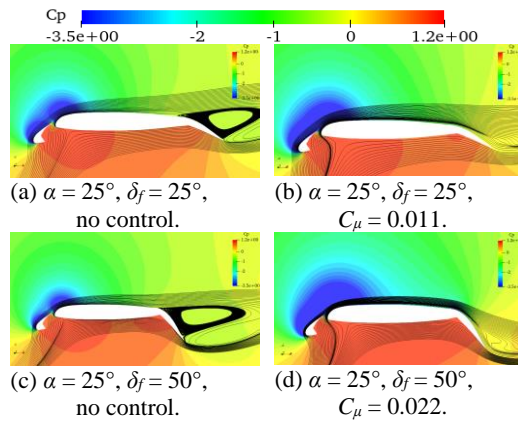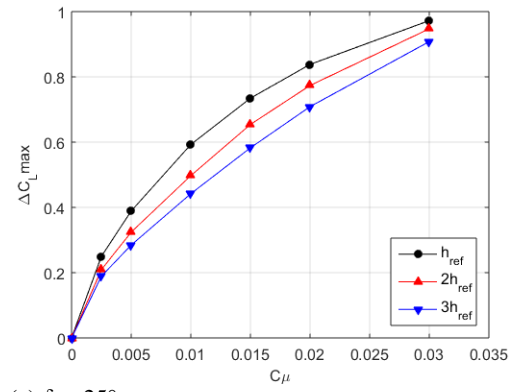
Fig. 14. Distribution of C_{Lmax} x C_μ.

(a) $\alpha = 25°$, $\delta_f = 25°$, no control.

(b) $\alpha = 25°$, $\delta_f = 25°$, $C_\mu = 0.011$.

(c) $\alpha = 25°$, $\delta_f = 50°$, no control.

(d) $\alpha = 25°$, $\delta_f = 50°$, $C_\mu = 0.022$.

Fig. 15. Streamlines and pressure coefficient contours over the airfoil.

(a) $\delta_f = 25°$.

(b) $\delta_f = 50°$.

Fig. 16. Lift gain (ΔC_{Lmax}) x C_μ.

attached to the flap surface. As the steady jet becomes stronger, the flow perturbations are attenuated and the streamlines tend to be more aligned to the body.

The flow behavior with the variation of the slot height, where the jet is applied, was also analyzed in this study. Variations with $2h$ and $3h$ were created, where $h = 0.085\%$ c. From the slot initially created with h, the flap was vertically translated downwards to create two more different configurations, with slot heights of 0.17% c and 0.255% c. This analysis was considered with different slot heights but the blowing momentum coefficient was kept the same. The total pressure at the boundary conditions was varied for each slot height and the changes were reflected in variation of velocity and density of the jet. Figure 16 shows the lift gains, $\Delta C_{Lmax} = (C_{Lmax} - C_{Lmax,C\mu=0})$, as a function of C_μ. Considering the two flap configurations, the higher differences of C_{Lmax} are found in the region close to the transition to super-circulation, $C_\mu = 0.011$ and 0.022, for flap at $25°$ and $50°$, respectively. This is because while the reference slot height h is close to the optimum performance where the flow is attached, the $2h$ and $3h$ slots are not, due to the differences in jet velocity. When all slot configurations present the super-circulation regime characteristics, the ΔC_{Lmax} values are close to each other (Fig. 16a). At $50°$ flap deflection (Fig. 16b), the ΔC_{Lmax} difference between $3h$ and h is still large after this region of transition for the reference
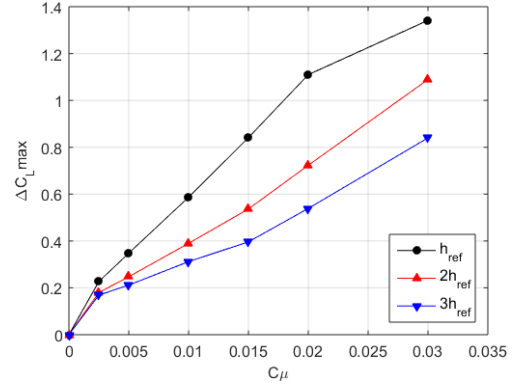
height h, reaching 0.50 at maximum C_μ. The remaining large difference at $C_\mu = 0.03$ can be explained by the fact that only the smaller slot presents the super-circulation regime. With the increase in C_μ the same trend is expected, as that which occurred in Fig. 16a for $\delta_f = 25°$, where the ΔC_{Lmax} values approach each other.

5.2. Unsteady Jet

The unsteady simulations with separation control begin with an analysis of the unsteady parameters, varying the time step discretization, related to the quantity of steps per jet period (20, 40 and 80 steps), and the number of iterations in each dual time step, 400 and 800, with CFL number fixed in 50. Considering a jet frequency of $f = 267$ Hz, or $T = 1/267$ s, 40 steps means a time step of 9.363×10^{-5} s. The case studied for time independency analysis is the sinusoidal jet with frequency of $F^+ = 1$ ($f = 267$ Hz), $\delta_f = 25°$, $\alpha = 20°$, $C_\mu = 0.005$.

The C_L evolution over the time can be viewed in Fig. 17. It was observed that the simulations with 40 steps (time step = 9.363×10^{-5} s) and 80 steps (time step = 4.682×10^{-5} s) per period and the number of iterations of 400 and 800 during each time step did not present significant differences in time-averaged C_L. The main differences are found between the curves of 40 and 80 steps and the curves with 20 steps. Table 4 shows the main results of this parameter analysis for
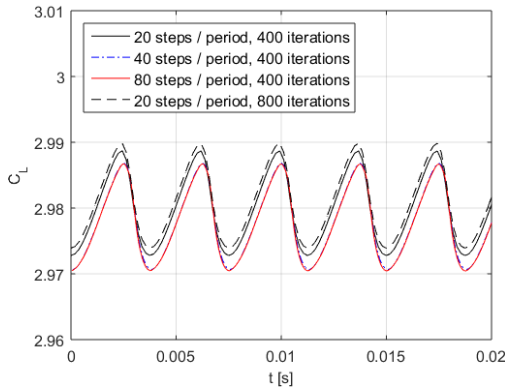
Fig. 17. Unsteady C_L after stabilization for different time-steps and number of iterations during each time-step, $C_\mu = 0.005$, $F^+ = 1$ ($f = 267$ Hz), $\delta_f = 25°$, $\alpha = 20°$.

$\delta f = 25°$. The curves with 20 steps per cycle (time step $= 1.8727 \times 10^{-4}$ s) and 800 iterations, and both 40 and 80 steps per cycle with 400 iterations present the same C_L amplitude, with a difference of the average value $\overline{C_L} = 0.003$ between the curves.

Therefore, the parameters were chosen with 40 steps per jet cycle (time step $= 9.363 \times 10^{-5}$ s) and 400 iterations in each time step as there is a good relationship between the quality of results and computational cost.

Once the parameters were established for the unsteady cases, one simulation with base flow (no control) for $\delta_f = 50°$ revealed a regular sinusoidal response of lift coefficient during the time with an amplitude of oscillation of 0.13 in relation to the average C_L of 1.63. From the FFT analysis for this configuration, a dominant vortex shedding with frequency of 80 Hz, or $F^+ = 0.33$ was observed, which can also be checked by the period length of C_L oscillations presented in Fig. 18.

Figure 19 shows the vortex shedding for the base flow and deployed flap at 50°. Four instantaneous plots are shown: at phase = 0°, 90°, 180° and 270°, where phase = 0° means the maximum C_L and 180° the minimum. In order to visualize the vortex shedding, the contours viewed in Fig. 19, are calculated as the difference between the free stream total pressure and the local total pressure, ΔP_0, where the change of energy can be clearly observed. Figure 19a shows the starting of the vortex shedding process, where a recirculation bubble is located over

Table 4 Average values and amplitude variation of C_L for different time-steps and number of iterations per time-step. Simulation parameters are given by $F^+ = 1$ ($f = 267$ Hz), $\delta_f = 25°$, $\alpha = 20°$, $C_\mu = 0.005$.

| Run	Iter. / Step	Time Step (s)	$\overline{C_L}$	C_L amp.
1	400	1.8727×10^{-4}	2.980	0.009
2	800	1.8727×10^{-4}	2.981	0.009
3	400	9.363×10^{-5}	2.978	0.009
4	400	4.682×10^{-5}	2.978	0.009
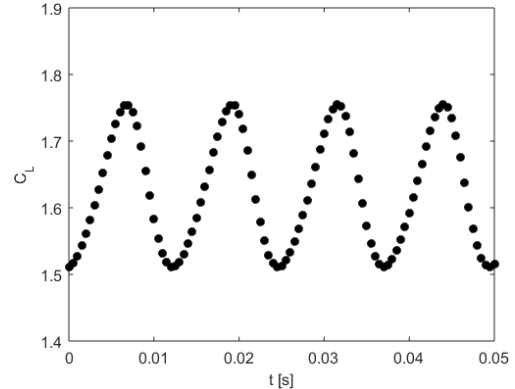
Fig. 18. C_L temporal signal obtained in the base flow simulation for $\delta_f = 50°$ configuration used as input data of FFT analysis, $\alpha = 0°$, no control, $\overline{C_L} = 1.63$.

the flap. For the 90° phase, the vortex starts rolling-up at the trailing edge (Fig. 19b), and grows in size (Fig. 19c) at the same time as the recirculation bubble is stretched shedding a weak vortex. Then, the trailing edge vortex is shedded and advected downstream, as can be seen in Fig. 19d, and the recirculation bubble recedes over the flap, restarting the vortex shedding dynamics.

Continuing the investigation of unsteady jets, a sinusoidal pulse employing $C_\mu = 0.005$ for $\delta_f = 25°$

ΔP_0 (Pa)

(a) Phase = 0°.

(b) Phase = 90°.

(c) Phase = 180°.

(d) Phase = 270°.
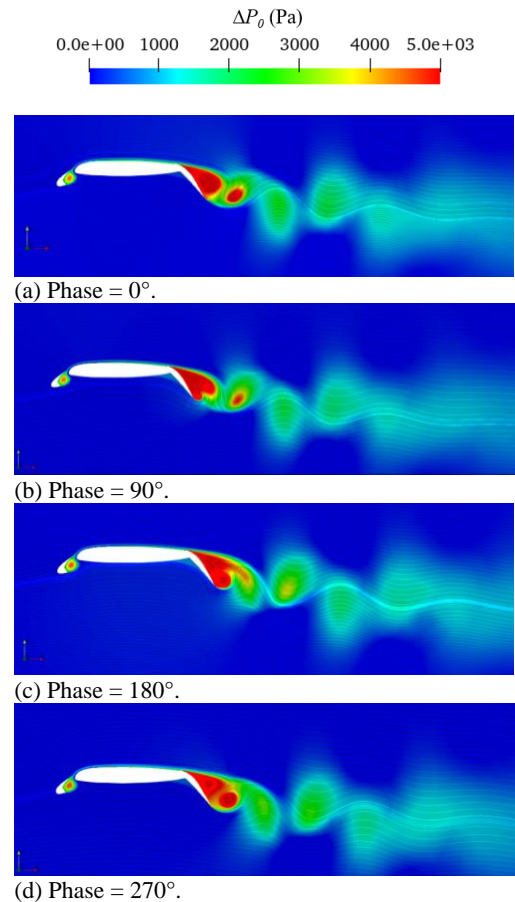
Fig. 19. Instantaneous ΔP_0 (Δtotal pressure, Pa) contour and streamlines plot for base flow of $\delta_f = 50°$ configuration, $\alpha = 0°$, no control.
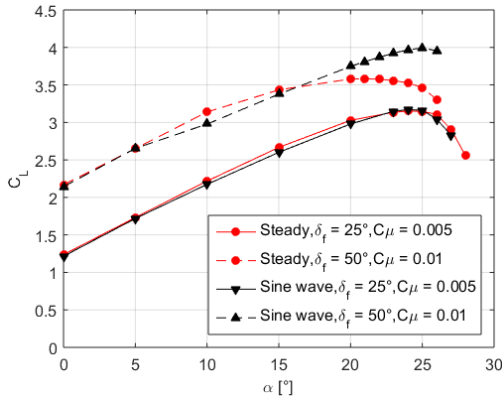
**Fig. 20.** C_L **x** α**, comparison of pulsed jet with sine waveform and steady jet.**

and $C_\mu = 0.010$ for $\delta_f = 50°$ were performed. Figure 20 shows the comparisons of steady and sinusoidal jets for $F^+ = 1$. For the case of $\delta_f = 25°$, no significant improvement was verified with pulsed jet. However, when we observe the results of $\delta_f = 50°$, the value of C_{Lmax} clearly increases and airfoil stall is delayed, changing from 22° to 25°.

Because of the different flap deflections and C_μ, values, it is difficult to conclude if the effect of the increase in C_L and stall delay for sinusoidal jets is related to higher flap deflections or higher C_μ values, or the combination of both. For this reason, an analysis was carried out at angle of attack fixed at 25°, varying the jet intensities C_μ (equal to 0.0025, 0.005, 0.01 and 0.015 for $\delta_f = 25°$ and 0.005, 0.01 and 0.015 for $\delta_f = 50°$) and the reduced frequencies F^+ (equal to 0.5, 1 and 2), as shown in Fig. 21. Regarding the jet frequency, when $C_\mu \geq 0.01$ the reduced frequency of $F^+ = 1$ and $F^+ = 2$ presented the highest ΔC_L for both flap configurations, although with a modest advantage in relation to $F^+ = 0.5$. With $C_\mu = 0.0025$, only $F^+ = 2$ equates the C_L gain of the steady jet for $\delta_f = 25°$ (Fig. 21a). With $C_\mu = 0.005$ all jets present similar gains, but when the flow field begins to reattach to the flap surface the lift gain is more evident with pulsed jets.

When we analyze the flap deflection of $\delta_f = 50°$ (Fig. 21b), the sinusoidal jet is more efficient than the steady jet for the whole range of C_μ studied, with emphasis on $C_\mu = 0.010$, where the larger difference of gain between the steady and pulsed jets was found. A reason for the difference at $C_\mu = 0.010$ for this $\delta_f = 50°$ configuration can be explained by the fact that the pulsed jet already presents the super-circulation regime, where the flow field around the airfoil is attached to the surface, unlike the steady jet, as can be seen in the flow comparisons in Fig. 22. For this $\delta_f = 50°$ configuration, it was observed that for the steady jet the super-circulation was achieved at $C_\mu = 0.022$ and for the pulsed jet, it occurred at $C_\mu = 0.010$ with peak values of $C_\mu = 0.020$ (Fig. 22c). So, the flow reattachment tends to be related to the peak velocity and not the average value of C_μ obtained during the jet period.

Besides analyzing the behavior of the C_L distributions applying sine waveforms, similar simulations with jets under square waveform were
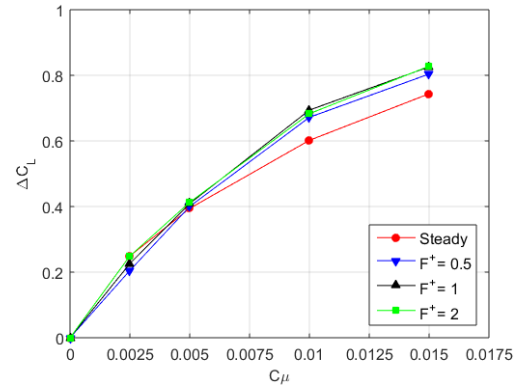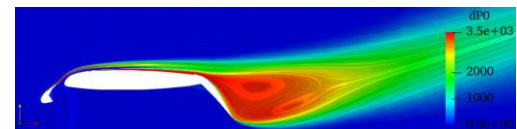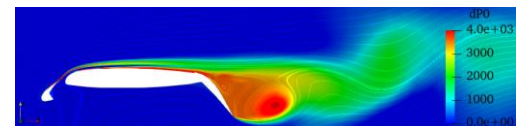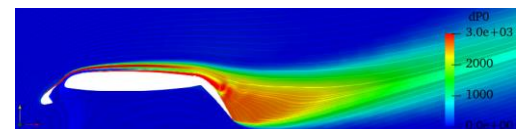

(a) $\delta_f = 25°$.
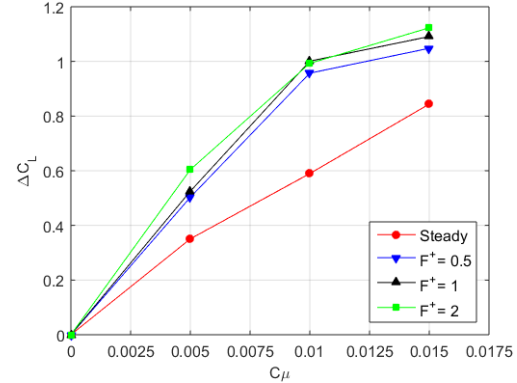
(b) $\delta_f = 50°$.

Fig. 21. Distribution of ΔC_L **x** C_μ **with reduced frequencies** F^+ **variations for sinusoidal waveform jets,** $\alpha = 25°$.


(a) $C_\mu = 0.010$, Steady jet.

(b) $C_\mu = 0.0025$, Pulsed jet.

(c) $C_\mu = 0.010$, Pulsed jet.

Fig. 22. Instantaneous ΔP_0 **(**Δ**total pressure, Pa) contour and streamlines plot for steady and pulsed jet with sine waveform and** $F^+ = 1$**,** $\delta_f = 50°$**,** $\alpha = 0°$**, Phase of maximum** C_L**.**

also performed, as shown in Fig. 23. Using the same parameters previously used for the sinusoidal jet, with $C_\mu = 0.005$ for $\delta_f = 25°$ and $C_\mu = 0.010$ for $\delta_f = 50°$, the curves are similar to those obtained in Fig. 20, with a small improvement in C_{Lmax} for $\delta_f = 25°$.
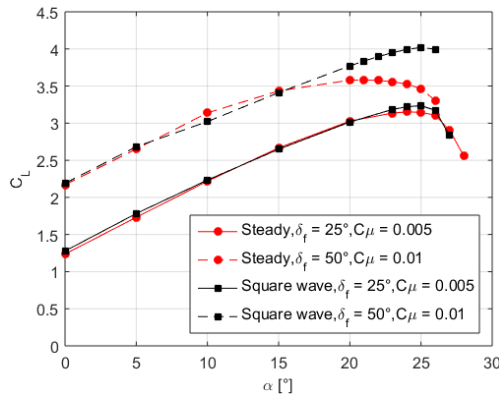
**Fig. 23. Comparison of pulsed jet with square waveform and steady jet.**

The C_{Lmax} obtained from sinusoidal was 3.17 versus 3.23 obtained from square wave, whereas for $\delta_f = 50°$ the C_{Lmax} improvement went from 3.99 to 4.02.

The influence of the variation of the reduced frequency and jet intensities on lift coefficient were also investigated for square waveform signal. Figure 24 shows the results of these variations for both flap deflections at fixed angle of attack of 25°. For flap deflected at 25° (Fig. 24a), small differences are found among F^+ values and also between steady and pulsed jets for $C_\mu = 0.0025$. After this point the pulsed jets are superior to steady jet for all reduced frequencies. We can observe that $F^+ = 0.5$, the closest frequency to natural vortex shedding, resulted in the lowest C_L gain for square waveform. No significant differences are found between $F^+ = 1$ and $F^+ = 2$ in the range of C_μ up to 0.015. For flap deflected at 50° (Fig. 24b) pulsed jets are superior to steady jets throughout the whole C_μ range, with the highest difference at $C_\mu = 0.010$, presenting a lift gain of 0.6 and around 1 for steady and pulsed jet respectively. Concerning the reduced frequencies, similar behavior was found for $\delta_f = 25°$ and $\delta_f = 50°$, with small differences between $F^+ = 1$ and $F^+ = 2$ and a lower gain for $F^+ = 0.5$.

Figure 25 shows a comparison of pressure coefficient distribution for different jets, for deployed flap at 50°, $C_\mu = 0.010$, $F^+ = 1$ in the cases of unsteady jets, and considering the respective angle of attack for maximum lift obtained from the $C_{L\alpha}$ curves. The increase of suction peak considering pulsed jets is around 70% in the slat and 30% in the main element, which resulted in larger differences between the
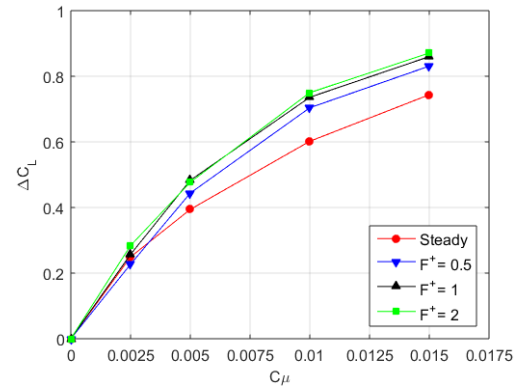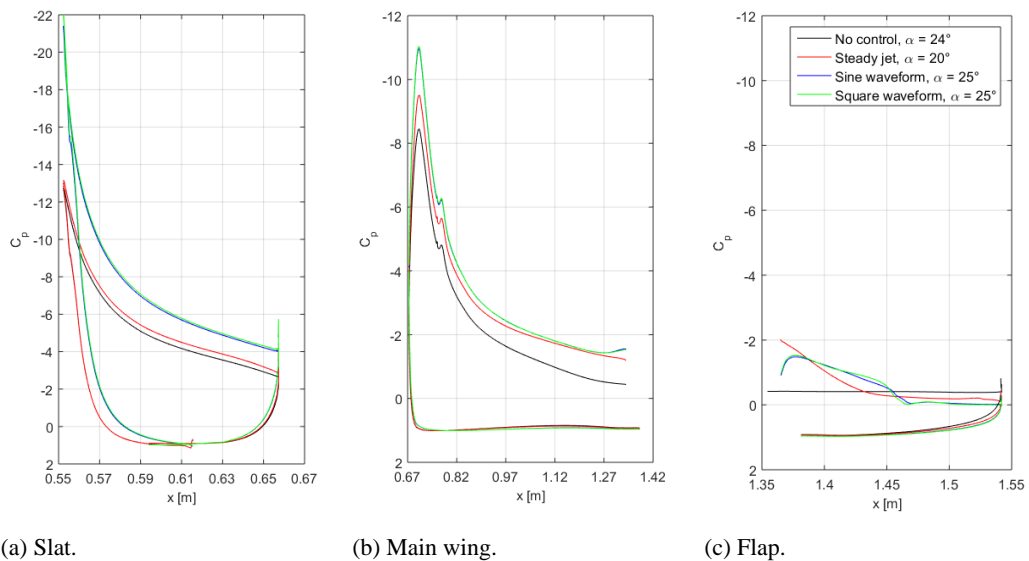

(a) $\delta_f = 25°$.
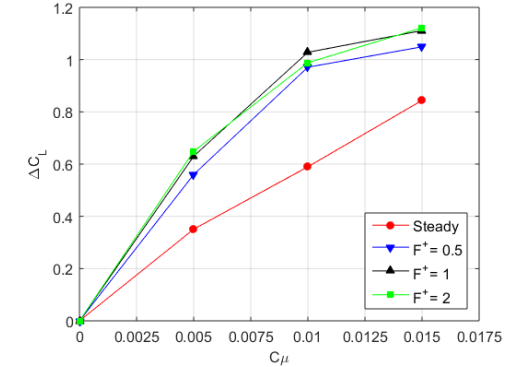
(b) $\delta_f = 50°$.

Fig. 24. Distribution of ΔC_L x C_μ with reduced frequencies F^+ variations for square waveform jets, $\alpha = 25°$.


(a) Slat.

(b) Main wing.

(c) Flap.

Fig. 25. Comparison of pressure coefficient distribution, $\delta_f = 50°$, $C_\mu = 0.01$.

curves from the lower and upper surfaces, and consequently led to a significant increase of lift. As the steady jet for this configuration presented a lower angle of stall, 20°, the effect of the slat is comparable to no control at $\alpha = 24°$. However, after the jump in pressure on the main element, the steady jet presents values of C_p close to that of the pulsed jets. Regarding the pressure distribution on the flap, this element is stalled with no control. When Active Flow Control is applied, pulsed jets proved superior with the exception of the initial part of the flap, where the steady jet presented a higher value of C_p magnitude although pulsed jets are set with higher peaks of C_μ.

Figure 26 shows the C_L time response to pulsed jets with both sinusoidal and square waveforms. It is clearly observed that the separation control diminished the amplitude of C_L response if compared to the amplitude of 0.13 obtained from the base flow (Fig. 18), with C_L amplitude around 0.04 in the worst case. Comparing the C_L responses for the two waveforms of pulsed jets, the square waveform presented a higher time-averaged C_L. On the other hand, it also presented a higher amplitude of C_L oscillations (approximately double the sine wave). Regarding the jet velocity at the outlet slot and the C_L response, there is a phase shift of $1/2$ T between the maximum jet velocities and the maximum C_L for both pulsed signals. Here, the jet period T is equal to the period of C_L response. For the square wave, the maximum C_L is achieved at the end of the duty cycle. After this, the C_L decays linearly following a sudden drop, while for the sinusoidal jet the C_L response apparently follows the pattern of its generated jet signal. We can also note that the response for this case reflects only the jet input frequency of 239 Hz, ensuring the destruction or at least the intensity attenuation of the vortices shedding initially obtained with 80 Hz, given that non visible changes of C_L occur in this range of frequency.

Another parameter analyzed was the mass flow for the jet types covered in this study. One of the main concerns of aircraft designers in using Active Flow Control is due to the high-pressure air supply. When synthetic jet actuators are not employed, the air supply comes from external sources such as engines, auxiliary power unit, APU, or dedicated compressors for the fluidic actuators. Besides taking into account
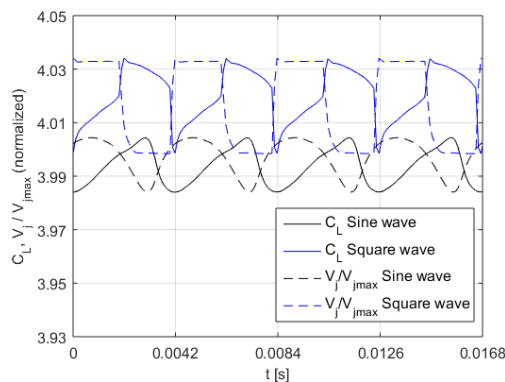
Fig. 26. C_L response to pulsed jets and normalized jet velocities, $\delta_f = 50°$, $\alpha = 25°$, $C_\mu = 0.01$, $F^+ = 1$.
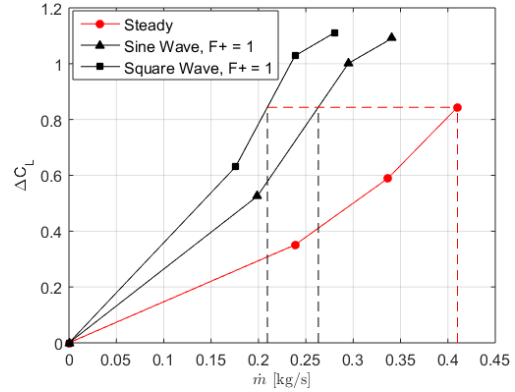
Fig. 27. Comparison of mass flow and C_L between steady and pulsed jets, $\delta_f = 50°$.

the aerodynamic performance optimization, the separation control system must be feasible and not compromise the regular running of the engine.

Therefore, the lift gain was also analyzed in relation to the mass flow. As the simulation is two-dimensional, the jet was considered over the full wingspan and at constant slot height to calculate mass flow.

The advantage of the application of pulsed jets over steady jets for flap deflection $\delta_f = 25°$ is also evidenced through mass flow analysis. Taking the same lift gain value from steady jet and $C_\mu = 0.015$, the reduction of mass flow is around 25.3% and 40.7% for sinusoidal and square wave, respectively. Cases of high deflected flap already have shown the benefits in terms of increase of lift and delay of the stall angle of attack using pulsed jets (Figs. 20 and 23). The superiority is even more evident when observing Fig. 27. A mass flow reduction around 35.8% and 48.9% for sinusoidal and square wave respectively is obtained for the same lift gain in relation to the steady jet.

Figure 28 presents the aerodynamic loads related to lift-to-drag (Fig. 28a) and drag polar (Fig. 28b) for steady and pulsed jets. From Fig. 28a, it can be observed that pulsed jet under square waveform presented superior efficiency compared to the other types of jet for both flap deflections, with an exception up to 10° angle of attack for $\delta_f = 50°$. It is also noted that the configuration with high flap deflection presents a more stable C_L/C_D throughout the variation of α for pulsed jets but is less efficient in terms of lift-to-drag. However, it cannot be misunderstood that the aerodynamic improvement is questionable once lower C_L/C_D values were found for $\delta_f = 50°$. In Fig. 28b comparisons between uncontrolled, steady and pulsed jets are shown. The reduction of drag and increase of lift using any type of AFC, where the curves were shifted to upper left is evident. But, within the flow control types the square waveform provided the best enhancements. For example, the configuration of $\delta_f = 25°$ demonstrated a lift gain of 17% and drag reduction of 16% when compared to uncontrolled case; and 36% of lift gain and 20% of drag reduction for $\delta_f = 50°$. With higher blowing momentum coefficient, $C_\mu = 0.015$, the lift gain was 38% and the reduction of
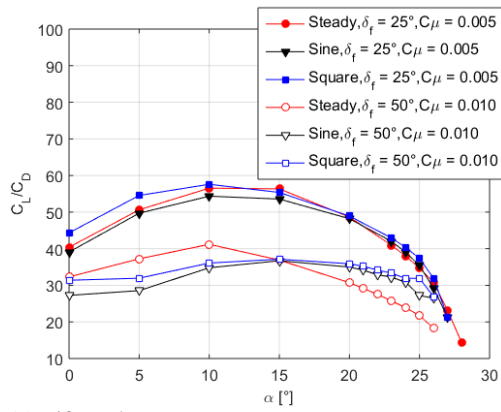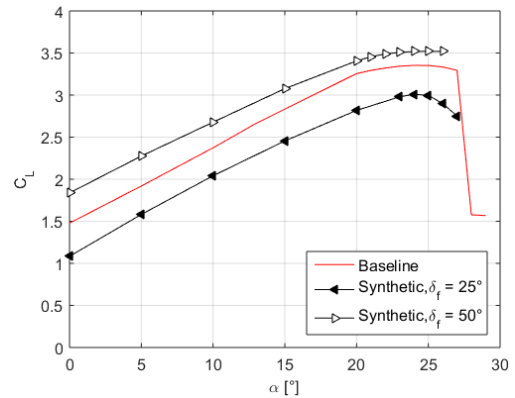
(a) Lift-to-drag **x** α.
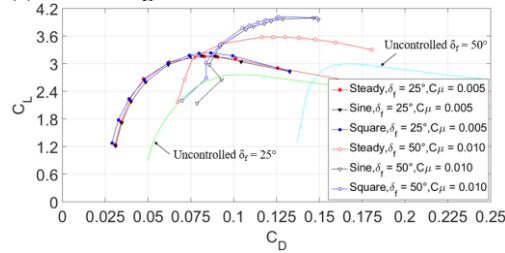
(b) Drag polar.

Fig. 28. Aerodynamic efficiency (C_L/C_D) for Pulsed and Steady jets.

Fig. 29. C_L x α, Synthetic jet.

Fig. 30. Synthetic jet, ΔC_L x F^+, $\alpha = 25°$.

drag was 10% at angle of attack of 25° for the same type of jet, as already shown in Fig. 24b. This confirms that there is an optimum combination regarding the flap deflection and the mass flow blowing. For higher C_μ values, only a small difference of lift gain and a lower reduction of drag were obtained. Regarding the results considering different waveforms, although the lift is very close between the sine and square waveforms, the drag is 15% lower when the square waveform was used.

The last analysis is related to the application of synthetic jets. Due to the limitations of the piezoelectric synthetic actuators, the aerodynamic analysis with synthetic jet was performed only with AFC at maximum peak jet velocity of $C_{\mu,peak} = 0.005$, giving an average velocity at the slot around 115 m/s. With this configuration the reduced frequency is set at $F^+ = 1$ and it is assumed that this is the diaphragm's natural resonance frequency. Afterwards, the reduced frequency is set at $F^+ = 0.5$ and $F^+ = 2$, making the same assumption regarding the natural resonance frequency.

The behavior of C_L as a function of the angle of attack for synthetic jet with pure sine signal and $F^+ = 1$ is shown in Fig. 29. With the maximum possible peak jet at the slot exit, the C_{Lmax} reached a value of 3.01 ($\alpha = 24°$) and 3.52 ($\alpha = 25°$) for $\delta_f = 25°$ and $\delta_f = 50°$, respectively. The C_{Lmax} value for $\delta_f = 25°$ is below the expectations, as the $C_{L\alpha}$ distribution is below the baseline. For $\delta_f = 50°$, C_{Lmax} is only 0.17 higher in relation to the baseline airfoil, which represents an increase in lift of 5%.

Figure 30 shows the value of the lift gain, ΔC_L for each of the reduced frequencies, $F^+ = 0.5, 1$ and 2.
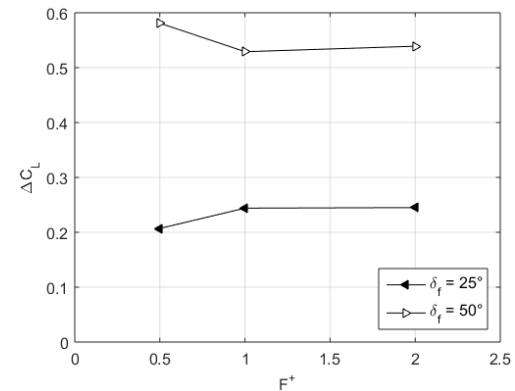
The highest ΔC_L is found with a reduced frequency of 1 and 0.5 for $\delta_f = 25°$ and $\delta_f = 50°$, respectively. It is interesting to note that the different flap deflections resulted in the opposite behavior of lift when $F^+ = 0.5$, where the minimum ΔC_L was obtained for $\delta_f = 25°$ and the maximum for $\delta_f = 50°$. Since the synthetic actuators operate at the resonance frequency to achieve their maximum efficiency, and consequently the maximum jet velocity, the optimized reduced frequency cannot be obtained for both flap configurations. This result leads to a difficulty in choosing the actuator to be applied to the wing. In respect of $F^+ = 1$ and $F^+ = 2$, the values are similar for each flap configuration, as also shown for pulsed jets.

Although synthetic jet has the benefit of eliminating the use of external pneumatic sources, the results presented in this study have shown that this technology limits its operational use when the main objective is the substitution of a conventional single slotted multi-element system. Since aircraft requires low flap deflection at take-off, synthetic jets (without the combination of any other type of jet) may not be adequate for this type of wing configuration.

6. CONCLUSIONS

Two-dimensional numerical simulations using SU2 code were carried out in order to analyze the performance of an airfoil with Active Flow Control, in comparison to a typical multi-element configuration. The results obtained in the present

work were based on the application of a tangential jet to the flap shoulder of a simplified high-lift system.

Combinations of different leading edge configurations with the modified plain flap equipped with AFC were simulated on NASA Trapezoidal Wing, where the most adequate configuration was shown to be the original baseline slat. With steady jet at C_μ of 0.03, the maximum C_L reached 3.73 and 4.34 at angles of attack of 25° and 19° for flaps deflected at 25° and 50°, respectively. Regarding the slot height analysis considering steady jet, smaller sizes lead to higher lift gains for the same C_μ values, with larger differences obtained close to the super-circulation regime.

One advantage of unsteady jets is that they provide gains similar to steady jets but use lower mass flow. This behavior was proven when pulsed jets under sinusoidal and square waveforms were simulated. For the same lift coefficient gain, the reduction of mass flow reached up to 35.8% and 48.9% for sinusoidal and square waveforms, respectively. The maximum C_L achieved the values of 3.61 for flap at 25° and 4.10 for flap at 50°, with a reduced frequency of $F^+ = 1$. An evaluation of the variation of reduced frequency, $F^+ = 0.5$, 1 and 2, was performed for both signals, where $F^+ = 1$ and $F^+ = 2$ values presented similar results and the highest value of C_L. Considering a C_μ of 0.010, pulsed jets postponed the angle of stall from 22° to 25° for deployed flap at 50°. For flap deflection of 25°, the angle of stall maintained the same value for both steady and pulsed jets. In summary, the square waveform presented a small superiority of C_L and a significant reduction in the required mass flow in relation to the sine waveform. For the highly deployed flap, the lift gain related to uncontrolled flow achieved 36% and a drag reduction of 20%. While sinusoidal and square waveforms reached similar lift enhancements, the drag is 15% higher for the sine wave. Nevertheless, despite the better aerodynamic improvements obtained with the square waveform, the amplitude of C_L oscillations observed during the AFC actuation periods, was approximately doubled**.**

Simulations for synthetic jets were carried out with jet velocity around 115 m/s. Even though the lift gain of 9% was obtained in relation to the uncontrolled case, the lift was lower than the baseline when the flap was deflected at 25°. With the flap deployed at 50°, an increase of 5% was obtained when compared to the baseline multi-component airfoil.

Based on the two-dimensional simulations, higher aerodynamic improvements were found with steady and pulsed jet with square waveform signal even with a highly deflected flap.

ACKNOWLEDGEMENTS

REFERENCES

Abbott, I. H. and A. Von Doenhoff (1959). *Theory of Wing Sections*. Dover Publications, Inc., New York.

Abramova, K. A., A.V. Petrov, A. V. Potapchik and V. G. Soudakov (2020). Experimental investigation of transonic buffet control on a wing airfoil using tangential jet blowing. *Fluid Dynamics* 55(4), 545-553.

Anders, S. G., W. L. Sellers III and A. E. Washburn (2004). Active flow control activities at NASA Langley. In *Proceedings of the 2nd AIAA Flow Control Conference*, Portland OR.

Bushnell, D. M. and I. Wygnanski (2020). Flow control applications. NASA/TM 220436.

Cattafesta, L. N. and M. Sheplak (2011). Actuators for active flow control. *Annual Review of Fluid Mechanics* (43), 247-272.

Celik, I. B.; U. Ghia, P. J. Roache and C. J. Freitas (2008). Procedure for estimating and reporting of uncertainty due to discretization in CFD applications. *Journal of Fluids Engineering* 130(7): 078001.

Chapin, V. G. and E. Bernard (2015). Active control of a stalled airfoil through steady or unsteady actuation jets. *Journal of Fluids Engineering* 137(9), 091103.

Ciobaca, V. and J. Wild (2013). An overview of recent DLR contributions on active flow-separation control studies for high-lift configurations. *Journal AerospaceLab* (6), 1-12.

Couluris, G. J., D. Signor and J. Phillips (2010). Cruise-efficient short takeoff and landing (CESTOL): potential impact on air traffic operations. *NASA/CR* 216392.

Crippa, S., S. Milber-Wilkending and R. Rudnik (2011). DLR Contribution to the first high lift prediction workshop. In *Proceedings of the 49th AIAA Aerospace Sciences Meeting including the New Horizons Forum and Aerospace Exposition*, Orlando FL.

Deere, K. (2003). Summary of fluidic thrust vectoring research at NASA langley research center. In *Proceedings of the 21st AIAA Applied Aerodynamics Conference*. Orlando FL, AIAA.

Delfs, J. W., C. Appel, P. Bernicke, C. Blech, J. Blinstrub, C. Heykena, P. Kumar, K. Kutscher, N. Lippitz, L. Rossian, L. Savoni and M. Lummer (2017). Aircraft and technology for low noise short take-off and landing. In *Proceedings of the 35th AIAA Applied Aerodynamics Conference*, Denver CO, AIAA.

DeSalvo, M., E. Whalen and A. Glezer (2020). High-lift performance enhancement using active flow

control. *AIAA Journal* 58(10), 1-15.

Diekmann, J. H. (2019). Flight mechanical challenges of STOL aircraft using active high-lift. *Journal of Aircraft* 56(5), 1-12.

Dods Jr., J. B. and E. C. Watson (1976). *The Effects of Blowing Over Various Trailing-Edge Flaps on an NACA 0006 Airfoil Section, Comparisons with Various Types of Flaps on Other Airfoil Sections, and an Analysis of Flow and Power Relationships for Blowing Systems*. NASA TN D-8293.

Durrani, N. and B. A. Haider (2011). Study of stall delay over a generic airfoil using synthetic jet actuator. In *Proceedings of the 49th AIAA Aerospace Sciences Meeting including the New Horizons Forum and Aerospace Exposition*, 2011, Orlando FL, AIAA.

Economon, T. D., F. Palacios, S. R. Copeland, T. W. Lukaczyk and J. J. Alonso (2016). SU2: An open-source suite for multiphysics simulation and design. *AIAA Journal* 54(3), 828-846.

Ekaterinaris, J. A. (2004). Prediction of active flow control performance on airfoils and wings. *Aerospace Science and Technology* 8(5), 401-410.

Englar, R. J. (1972). Two-dimensional subsonic wind tunnel investigations of a cambered 30 percent thick circulation control airfoil. *Naval Ship Research and Development Center* AD913411.

Englar, R. J. and G. G. Huson (1983). Development of advanced circulation control wing high lift airfoils. In *Proceedings of the AIAA Applied Aerodynamics Conference*, Danvers MA, AIAA.

Goffert, B., R. G. Silva, C. P. F. Francisco, E. Pigusov, C. Wei, Z. Qian and M. L. C. C. Reis (2021). Numerical study of a wing section with a tangential blowing jet control system. In *Proceedings of CHT-21 ICHMT International Symposium on Advances in Computational Heat Transfer*, Online, CHT-21-169.

Greenblatt, D., I. J. Wygnanski and C. L. Rumsey (2010). *Aerodynamic Flow Control, Encyclopedia of Aerospace Engineering*. John Wiley & Sons, Ltd.

Hannon, J. A., A. E. Washburn, L. N. Jenkins and R. D. Watson (2012). Trapezoidal wing experimental repeatability and velocity profiles in the 14- by 22-Foot Subsonic Tunnel (Invited). In *Proceedings of 50th AIAA Aerospace Sciences Meeting Including the New Horizons Forum and Aerospace Exposition*, Nashville TN, AIAA.

Hartwich, P. M., P. P. Camacho, K. El-Gohary, A. B. Gonzales, E. L. Lawson and A. Shmilovich (2017). System-level trade studies for transonic transports with active flow control (AFC) enhanced high-lift systems. In *Proceedings of 55th AIAA Aerospace Sciences Meeting*, Grapevine TX, AIAA.

Haucke, F. and W. Nitsche (2013). Active flow control on the flap of a 2D high-lift wing section towards high Reynolds number application. In *Proceedings of 31st AIAA Applied Aerodynamics Conference*, San Diego CA, AIAA.

Hogue, J., M. Brosche, W. Oates and J. Clark (2009). Development of a piezoelectric supersonic microactuator for broadband flow control. In *Proceedings of the Florida Center for Advanced Aero-Propulsion Conference*, Tallahassee FL.

Holl, T., A. K. vel Job, P. Giacopinelli and F. Thiele (2012). Numerical study of active flow control on a high-lift configuration. *Journal of Aircraft* 49(5), 1406-1422.

Hue, D., C. François, J. Dandois and A. Gebhardt (2017). Simulations of an aircraft with constant and pulsed blowing flow control at the engine/wing junction. *Aerospace Science and Technology* (69), 659-673.

Johnson, P. L., K. M. Jones and M. D. Madson (2000). Experimental investigation of a simplified 3D high lift configuration in support of CFD validation. In *Proceedings of 18th AIAA Applied Aerodynamics Conference and Exhibit*, Denver CO, AIAA.

Jones, G. S., C. S. Yao and B. G. Allan (2006). Experimental investigation of a 2D supercritical circulation-control airfoil using Particle Image Velocimetry. In *Proceedings of the 3rd AIAA Flow Control Conference*, San Francisco CA, AIAA.

Jones, G. S., J. C. Lin, B. G. Allan, W. E. Milholen, C. L. Rumsey and R. C. Swanson (2008). Overview of CFD validation experiments for circulation control applications at NASA. In *International Powered Lift Conference*, London.

Jones, G. S., W. E. Milholen, D. T. Chan, S. L. Goodliff, C. M. Cagle and J. S. Fell (2018). A discrete and distributed steady blowing application on high Reynolds number semispan supercritical wing configuration (Invited). In *Proceedings of the 2018 AIAA Aerospace Science Meeting*, Kissimmee FL, AIAA.

Kauth, F., D. G. François, Y. E. Sayed, R. Semaan, C. Behr, M. Schwerter, M. Leester-Schädel, V. Srinivas, F. Nolte, G. Narjes, J. Müller, C. Atalayer, D. Giesecke, T. Müller, R. Radespiel and J. R. Seume (2017). Progress in efficient active high-lift. In *Proceedings of the 35th AIAA Applied Aerodynamics Conferenc*e, Denver CO, AIAA.

Lawford, J. A. and D. N. Foster (1969). Low-Speed Wind Tunnel Tests on a Wing Section with Plain Leading- and Trailing-Edge Flaps Having Boundary-Layer Control by Bowing, Reports and Memoranda N. 3639. London Her Majesty's Stationery Office.

Lin, J. C., L. P. Melton, J. A. Hannon, M. Y. Andino, M. Koklu, K. B. Paschal and V. N. Vatsa (2019). Wind tunnel testing of active flow control on high-lift common research model. In *Proceedings of AIAA Aviation 2019 Forum*, Dallas TX, AIAA.

Lin, J. C., L. P. Melton, S. A. Viken, M. Y. Andino, M. Koklu, J. A. Hannon and V.N Vatsa (2017). High lift common research model for wind tunnel testing: an active flow control perspective. In *Proceedings of 55th AIAA Aerospace Sciences Meeting*, Grapevine TX, AIAA.

Liu, Y., L. N. Sankar, R. J. Englar, K. K. Ahuja and R. Gaeta (2004). Computational evaluation of the steady and pulsed jet effects on the performance of a circulation control wing section. In *Proceedings of 42nd AIAA Aerospace Sciences Meeting and Exhibit*, Reno NV, AIAA.

Liu, Z. and G. Zha (2016). Transonic airfoil performance enhancement using co-flow jet active flow control. In *Proceedings of 8th AIAA Flow Control Conference*, Washington-DC, AIAA.

Liu, Z., Z. Luo, Q. Liu and Y. Zhou (2020). Modulation of driving signals in flow control over an airfoil with synthetic jet. *Chinese Journal of Aeronautics* 33(12), 3138-3148.

Masiol, M. and R. M. Harrison (2014). Aircraft engine exhaust emissions and other airport-related contributions to ambient air pollution: A review. *Atmospheric Environment* (95), 409-455.

Melton, L. P., M. Koklu, M. Andino and J. C. Lin (2018). Active flow control via discrete sweeping and steady jets on a simple-hinged flap. *AIAA Journal* 56(8), 2961-2973.

Menter, F. R. (1994). Two-equation eddy-viscosity turbulence models for engineering applications. *AIAA Journal* 32(8), 1598-1605.

Meredith, P. T. (1993). Viscous phenomena affecting high-lift systems and suggestions for future CFD development. High-Lift System Aerodynamics, AGARD CP-515, 19/1-8.

Oberkampf, W. L. and C. J. Roy (2010). *Verification and Validation in Scientific Computing*. Cambridge University Press.

Palacios, F., T. D. Economon, A. Aranake, S. R. Copeland, A. K. Lonkar, T. W. Lukaczyk, D. E. Manosalvas, K.R. Naik, S. Padron, B. Tracey, A. Variyar and J. J. Alonso (2014). Stanford university unstructured (su2): analysis and design technology for turbulent flows. In *Proceedings of the 52nd Aerospace Sciences Meeting*, National Harbor MD. AIAA.

Pavlenko, O., A. Petrov and E. Pigusov (2018). Concept of medium twin-engine STOL transport airplane. In *Proceedings of 31st Congress of the International Council of the Aeronautical Sciences*, Belo Horizonte, Brazil, ICAS 2018-0104.

Petrov, A. V. (2012). Aerodynamics of STOL airplanes with powered high-lift systems. In *Proceedings of the 28th Congress of the International Council of the Aeronautical Sciences*, Brisbane, ICAS 2012-9.5.2.

Radespiel, R., M. Burnazzi, M. Casper and P. Scholz (2016). Active flow control for high lift with steady blowing. *The Aeronautical Journal* 120(1223), 171-200.

Rosenblum, J. P., P. Vrchota, A. Prachar, S. H. Peng, and S. Wallin (2019). Active flow separation control at the outer wing. *CEAS Aeronautical Journal*.

Rudolph, P. K. C. (1996). High-Lift Systems on Commercial Subsonic Airliners. NASA Contractor Report 4746.

Rumsey, C. L. and J. Hannon (2011). Description of transformations between stowed and un-stowed coordinates.https://hiliftpw.larc.nasa.gov/Work shop1/stowing-unstowing.txt.

Rumsey, C. L., J. P. Slotnick, M. Long, R. A. Stuever and T. R. Wayman (2011). Summary of the first AIAA CFD High-Lift Prediction Workshop. *Journal of Aircraft* 48(6), 2068-2079.

Rumsey, C. L., T. B. Gatski, S. X. Ying and A. Bertelrud (1997). Prediction of high-lift flows using turbulent closure models. In *Proceedings of the 15th AIAA Applied Aerodynamics Conference*, Atlanta GA, AIAA.

Salimi, M. R., R. Askari and M. Hasani (2022). Computational investigation of effects of side-injection geometry on thrust-vectoring performance in a fuel-injected dual throat nozzle. *Journal of Applied Fluid Mechanics* 15(4).

Seifert, A., A. Darabi and I. Wygnanski (1996). Delay of airfoil stall by periodic excitation. *AIAA Journal* 33(4), 691-698.

Seifert, A., T. Bachar, D. Koss, J. M. Shepshelovich and I. Wygnanski (1993). Oscillatory blowing: a tool to delay boundary layer separation. *AIAA Journal* 31(11), 2052-2060.

Sellers III, W. L., G. S. Jones and M. D. Moore (2002). Flow control research at NASA Langley in support of high-lift augmentation. In *Proceedings of 2002 Biennial International Powered Lift Conference and Exhibit*, Williamsburg VA, AIAA.

Shmilovich, A., Y. Yadlin and E. A. Whalen (2018). Active flow control computations: from a single actuator to a complete airplane. *AIAA Journal* 56(12), 4730-4740.

Singh, D. K., A. Jain and A. R. Paul (2021). Active flow control over a NACA23012 airfoil using hybrid jet. *Defence Science Journa* 71(6), 721-729.

Slotnick, J. P., J. A. Hannon and M. Chaffin (2011). Overview of the first AIAA CFD high lift prediction workshop. In *Proceedings of the 49th AIAA Aerospace Sciences Meeting including the New Horizons Forum and Aerospace Exposition*, Orlando FL, AIAA.

Spalart, P. and S. Allmaras (1992). A one-equation turbulence model for aerodynamic flows. In *Proceedings of the 30th Aerospace Sciences Meeting and Exhibit*, Reno NV, AIAA.

Tesar, V., C. Hung and W. Zimmerman (2006). No-moving-part hybrid-synthetic jet actuator, *Sensors Actuators A: Physical* 125(2), 159-169.

Washburn, A. E., S. A. Gorton and S. G. Anders (2002). Snapshot of active flow control research at NASA Langley. In *Proceedings of 1st Flow Control Conference*, Saint Louis MO, AIAA.

Wild, J. (2020). Editorial for the CEAS aeronautical journal special issue on active flow control research within the AFLoNext project. *CEAS Aeronautical Journal* (11), 803-804.